Revision 1 10110 words

Significance of tridymite distribution during cooling and vapor-phase alteration of ignimbrites

YULI HELED[1], MICHAEL C. ROWE[1*], ISABELLE CHAMBEFORT[2], COLIN J.N. WILSON[3]

[1]SCHOOL OF ENVIRONMENT, UNIVERSITY OF AUCKLAND, AUCKLAND, NEW ZEALAND, 1142.
[2]GNS SCIENCE, WAIRAKEI RESEARCH CENTRE, TAUPO 3384, NEW ZEALAND
[3]SCHOOL OF GEOGRAPHY, ENVIRONMENT AND EARTH SCIENCES, VICTORIA UNIVERSITY OF WELLINGTON, WELLINGTON 6140, NEW ZEALAND

*Corresponding author: Tel (+64) 9 923 6681; Michael.rowe@auckland.ac.nz

Key Words: tridymite, cristobalite, crystallization, devitrification, vapor-phase alteration, Whakamaru ignimbrite, Bishop Tuff, Grey's Landing ignimbrite

For submission to American Mineralogist

ABSTRACT

Thick sequences of silicic ignimbrites contain complex emplacement and cooling histories, often masking contacts between ignimbrite flow packages. Mineralogical and textural variations in these sequences are primarily a function of emplacement temperature and cooling time. Here, we focus on the use of the silica polymorph tridymite to understand the association of vapor-phase crystallization and devitrification within ignimbrite flow packages. As opposed to the common occurrence of cristobalite, the restricted domains in which we observe tridymite may provide more relevant constraints for interpreting post-emplacement devitrification and vapor-phase alteration. This study examines sections through the Whakamaru (New Zealand), Bishop (USA), and Grey's Landing (USA) ignimbrites by combining textural observations with measurements of density, groundmass crystallinity, and the distribution and proportion of tridymite to cristobalite. The rheomorphic Grey's Landing ignimbrite represents a high-temperature endmember scenario, with widely distributed tridymite (up to 20%) resulting from a high magmatic temperature and rapid devitrification in a low porosity deposit. In the welded Whakamaru and Bishop ignimbrites, metastable tridymite (up to 13%) is concentrated along boundaries between flow packages. Here tridymite is interpreted to crystallize in transient permeable zones, forming during vapor-phase alteration prior to compaction, where upper denser-welded flow materials serve as vapor seals. Our results suggest that tridymite may link the initial cooling and welding history of ignimbrites to vapor-phase alteration and devitrification, and may serve as a potential mineralogical fingerprint of depositional contacts, important for consideration of lateral transport of fluids in geothermal reservoirs.

INTRODUCTION

Ignimbrites, the deposits of concentrated pyroclastic flows, show a great range in lithological characteristics linked to their emplacement and cooling histories. These characteristics relate to both the mechanical processes involved in flow emplacement and the consequent thermal characteristics of the resulting deposits (e.g. Smith 1960a,b; Ross and Smith 1961; Streck and Grunder 1995; Grunder and Russell 2005; Quane and Russell 2005; Branney et al. 2008; Wright and Cashman 2014). In particular, ignimbrite welding textures correlate to emplacement temperatures (reflected in the rock density: Wilson and Hildreth 2003), varying from non-welded (low temperature; McClelland et al. 2004) to densely-welded with rheomorphic flow (high temperature; Branney et al. 2008).

In parallel with the variations in thermal histories seen in density/welding intensity, there is frequently a transformation of the amorphous glass phase by devitrification and vapor-phase alteration (Smith 1960; Streck and Grunder 1995; Keating 2005; Wright et al. 2011). Here we adopt simple definitions of devitrification and vapor-phase alteration following prior work on the Whakamaru ignimbrite by Briggs (1976a). Devitrification, the crystallization of the amorphous glass phase, occurs below the glass transition temperature (Lofgren 1971). Vapor-phase alteration in contrast is associated with crystals forming in voids or open spaces (Briggs 1976a). The timing and extent of vapor-phase alteration is dependent on temperature changes, and the source and availability of volatiles (Sheridan 1970; Keith 1991). Field investigations have documented the relative timing and relationship between devitrification and vapor-phase alteration, whereby in many cases volatiles released from glass during devitrification promote vapor-phase alteration in the mid- to upper levels of the ignimbrite (Sheridan 1970; Streck and Grunder 1995).

This study focuses primarily on the relationship between post-depositional crystallization and emplacement history of the Whakamaru (NZ) and Bishop (USA) ignimbrites. The Grey's Landing ignimbrite (Andrews and Branney, 2011), a high-

temperature Snake-River Plain (SRP)-type ignimbrite, provides a textural and mineralogical endmember (Ellis et al. 2015) where crystallization patterns reflect devitrification in a low porosity deposit with little pore space available for vapor-phase crystallization.

The mineralogical changes accompanying devitrification and vapor-phase alteration provide insights into post-eruptive processes such as cooling, crystallization, and degassing. These processes in turn are important in understanding fluid flow and reactions in ignimbrites in situations such as geothermal reservoir modelling (Cavazos-Álvarez et al. 2020) and flow of groundwater through underground repositories (Spycher et al. 2003). While the silica polymorph cristobalite has received a great deal of attention because of its widespread occurrence in volcanic deposits and carcinogenic properties (Schipper et al. 2020), we suggest the more restricted domains in which tridymite is observed in ignimbrites may provide a more targeted fingerprint for interpreting ignimbrite emplacement and cooling processes.

Tridymite stability has been debated since the early work of Fenner (1913), with experimental observations suggesting important temperature and compositional controls (e.g. Holmquist 1961; Flörke and Langer 1972). Stevens et al. (1997) argued for what is now generally accepted: tridymite stability is dependent on chemical impurities such as water or alkali oxides, with the amount and type of oxide influencing crystallization temperatures (β-tridymite stable starting from 870-1000 °C: Holmquist 1961) and kinetics (Garofalini and Miller 1986). Tridymite is generally considered a metastable phase at lower temperatures (Jones and Segnit 1972), with both metastable cristobalite and tridymite favored by rapid growth rates from amorphous silica. It is suggested that both cristobalite and tridymite initially nucleate, with higher rates of nucleation initially favoring cristobalite, but giving way to tridymite as crystallization progresses (Madden and Van Vlack 1967; Wu et al. 2002). The balance between the proportions of the silica polymorphs formed through devitrification and

vapor-phase processes thus may give us information about the post emplacement history of ignimbrites (Payette and Martin 1986; Green and Fitz 1993; Rowe et al. 2012). We therefore investigate the contrasts in silica polymorph development and significance of tridymite occurrences from both devitrification and vapor-phase alteration in the Whakamaru ignimbrite, Bishop Tuff, and Grey's Landing ignimbrite, representing a range of eruption temperatures and emplacement histories.

GEOLOGIC BACKGROUND

This study uses samples from three supereruption-related ignimbrites, Whakamaru (NZ), Bishop (USA), and Grey's Landing (USA; Fig. 1). The 0.35 Ma Whakamaru ignimbrite erupted as part of a sequence of voluminous tuffs (>1000 km^3; Whakamaru Group) accompanying the formation of the largest caldera in the central Taupo Volcanic Zone of New Zealand (Fig. 1A; Wilson et al. 1986; Brown et al. 1998, Downs et al. 2014). Northwest of the caldera, the Whakamaru ignimbrite forms a thick (locally >200 m) infill along the paleovalley of the Waikato River (Martin 1965). This infill has since been partially eroded by the river along the line of the pre-ignimbrite valley. Although varying degrees of welding intensity are evident across flow packages, no non-welded parts exposed in this area have survived weathering (Briggs 1976a, b). A chronology for the ignimbrite has not been established: although a widespread co-eruptive fall deposit has been identified beyond the limits of the ignimbrite (Froggatt et al. 1986; Matthews et al. 2012), fall deposits have never been reported underlying, interbedded with or overlying the ignimbrite itself. Estimated magmatic temperatures derived from Fe-Ti oxide pairs indicate several different pumice populations that record temperatures from 740 to 840 °C (Brown et al. 1998), while amphibole compositions yield a similar temperature mode of 770 °C (Matthews et al. 2012).

However, Brown et al. (1998) suggest magmatic temperatures from the Whakamaru ignimbrite relevant to this study are at the lower end of that temperature spectrum.

Within the Maraetai dam section of the Whakamaru ignimbrite along the Waikato River, early workers defined a region of dominant horizontal fracturing (Fig. 1) as a contact between ignimbrite packages within the deposit (e.g. Ewart 1965; Martin 1965). The upper package, as defined by Martin (1965) has a higher crystal and pumice content, although the contact is described as gradational. In contrast, Briggs (1976b) cast the Whakamaru ignimbrite into six subunits (A-F) based on textural, mineralogical, and magnetic properties. On this basis, and the Maraetai dam section would be composed primarily of subunits D, E, and the lower portion of F as defined by her. Briggs (1976b) argued that the horizontal jointing occurs at the transition from dense to moderate welding, rather than at the lithologic contact between flow packages (Fig. 2, Supplemental Figure 1).

The 0.76 Ma Bishop Tuff was erupted accompanying formation of Long Valley caldera in eastern California, representing the culmination of a prolonged history of silicic volcanism in the area (Hildreth 2004; Hildreth and Fierstein 2017). The eruption generated widespread fall deposits and a large, partly welded ignimbrite in a short-lived eruption, estimated to have lasted of the order of a week from consideration of accumulation rates for the fall deposits that are demonstrably coevally emplaced with the ignimbrite (Wilson and Hildreth 1997; Hildreth and Wilson 2007). The fall deposit is subdivided into nine units (F1-F9), in places interbedded with the ignimbrite which itself is divided into early (Ig1) and late (Ig2) flow packages, labelled with an indicator of where the deposit is best developed (Ig2E), and subpackages (a, b, c, d; Wilson and Hildreth 1997). Stratigraphic descriptions of the Bishop Tuff are detailed in Wilson and Hildreth (1997, 2003). Magmatic temperatures are inferred to range from 715 – 820 °C based on Fe-Ti oxides, generally increasing from earlier- to later-erupted material, with the lower ignimbrite (Ig1) less than approximately 765

°C (Hildreth and Wilson 2007). Along the Owens Gorge, welding rank varies from non-welded to densely welded. Proximal and distal sections are dominated by non-welded or sintered ignimbrite. Medial sections are dominantly welded to densely welded ignimbrite, with heterogeneous welding patterns associated with the two main ignimbrite flow packages (Ig1 and Ig2; Wilson and Hildreth 2003).

Providing contrast to the Whakamaru and Bishop deposits, the ~8 Ma Grey's Landing ignimbrite is part of the 10.6-8 Ma Rogersons Formation in southern Idaho (Fig. 1C; USA), and representative of SRP-type ignimbrites (Fig 1; Branney et al. 2008). Among other features, the Grey's Landing ignimbrite preserves unusually intense welding and rheomorphism associated with a relatively dry magma and high eruption temperature (900-1000 °C: Andrews et al. 2008; Ellis et al. 2010). The Grey's Landing ignimbrite shows variations in thickness from 3 to 75 m, reflecting the underlying paleotopography (Andrews and Branney 2011; Ellis et al. 2015). The 50 m thick Backwaters section of the Grey's Landing ignimbrite has 2-3 m of black, glassy basal vitrophyre, transitioning rapidly into 45 m of crystalline ignimbrite with rheomorphic flow banding, and topped with a thin upper vitrophyre. This material is now correlated with deposits in other areas to yield a proposed volume of 2800 km^3 (Knott et al. 2020).

METHODS

Samples from the Whakamaru, Bishop, and Grey's Landing ignimbrites are used here. New analytical results are combined with literature data to provide a more comprehensive assessment of the three deposits. A summary of analytical approaches for each sample is detailed in Supplementary Table 1.

Sampling sites and materials

Whakamaru samples used for this study were collected adjacent to Maraetai dam on the Waikato River, New Zealand (Figs. 1A and 2). For stratigraphic and lithologic descriptions of the full Whakamaru section (only accessible with drill core) see Martin (1965). Thirteen samples were collected at semi-regular intervals through the near continuous ~50 m thick section exposed adjacent to the Maraetai power station. Sample numbers 16MD-1 to 16MD-9 were collected along a single road exposure immediately below the dam. An additional four samples (16MD-11 to 16MD-14) were collected through a 14 m section immediately above the dam along a separate road exposure (Sample 16MD-10 is not utilized due to a higher degree of weathering and difficulty in placing it in stratigraphic context). Sampling was intentionally targeted to coincide with changes in fracture patterns, qualitatively described based on their relative predominant orientation and measured spacing (Fig. 2B). Effort was taken to obtain representative bulk samples at each locality, avoiding surfaces with pervasive fracturing which may have experienced more significant vapor phase alteration.

Bishop Tuff samples used for this study are from Wilson and Hildreth (2003) (Fig. 1B). Samples were collected from measured stratigraphic sections B, G, and H along the walls of Owens Gorge, southeast of the caldera, presented in Wilson and Hildreth (2003) (Fig. 1B; see simplified stratigraphic sections in Supplemental Figure 1). Sections G (132 m) and H (134 m) have a similar stratigraphy, both encompassing roughly equal proportions of ignimbrites Ig1Eb and Ig2Eb. However, section H includes ~5m of ignimbrite Ig2Ea and fall deposits F8 and F9. Section B (162m) includes ~80 m of both Ig1Ea and Ig1Eb with ~ 1m of fall deposit F6 midway through the section (Wilson and Hildreth 2003).

X-ray diffraction patterns from the Backwaters section of the Grey's Landing ignimbrite presented in Ellis et al. (2015) are reprocessed here for quantitative mineralogy and combined with backscattered electron (BSE) imaging. Groundmass crystallinity results

224 are from Ellis et al. (2015). Stratigraphy for this section is presented in Andrews and Branney
225 (2011) and Ellis et al. (2015). Samples through the Backwaters section were collected
226 generally every 4m through the crystalline core with increasing sampling density near
227 transitions to the upper and lower vitrophyre (Ellis et al. 2015).
228
229 **Imaging**
230 BSE images were collected from representative Whakamaru and Bishop (section G)
231 thin sections and polished 25 mm diameter epoxy rounds, respectively. Images were utilized
232 to identify groundmass textures and mineral phases (alkali feldspar and silica phases). For
233 image analysis the thin sections were either carbon-coated or gold-coated and analyzed with a
234 JEOL Neoscope JCM-6000plus Benchtop Scanning Electron Microscope (SEM) with an
235 energy dispersive spectrometer (EDS) at GNS Science, Wairakei Research Centre. Grey's
236 Landing ignimbrite BSE images were collected from carbon-coated polished 25 mm diameter
237 epoxy rounds, on a JEOL 8500F field emission -electron microprobe (FE-EMPA) at
238 Washington State University.
239
240 **Mineralogy**
241 Crystallinity measurements were made on a PANalytical Empyrean powder X-ray
242 diffractometer with a Cu X-ray tube (Cu $K\alpha_1$ 1.5406Å) at the University of Auckland.
243 Samples were analyzed from 5° to 50° 2Θ, with an integrated dwell time of 144 sec/step
244 (0.026° 2Θ step size) on a PIXcel 1D detector (strip detector) with attached graphite
245 monochronometer (following the methodology of Zorn et al. 2015). Handpicked, phenocryst-
246 free groundmass, bulk ignimbrite, and sieved fines from Whakamaru ignimbrite samples
247 were analyzed following XRD preparation methodologies described by Rowe et al. (2012).
248 For Bishop ignimbrite samples, only phenocryst-free groundmass was analyzed following the

same methodology. Crystallinity from XRD patterns is determined using the statistical freeware AMORPH (Rowe and Brewer 2008). Measured crystallinities are calibrated based on a mixture of granite and glass, varying in 10% proportions (Fig. 3). A third-order polynomial best fit is used for the calibration curve, accounting for the decrease in signal-noise at low crystallinities (<10%), and apparent peak broadening resulting from overlapping diffraction peaks at high crystallinities (>90%). Crystallinity methods for the Grey's Landing ignimbrite samples are reported in Ellis et al (2015) and Supplementary Table 1, following the procedure of Rowe et al (2012). Ellis et al. (2015) utilized the same basic methodology employed in this study, except that background fitting was conducted manually using the Jade software package, rather than with the AMORPH program.

Using the same diffraction patterns as for the crystallinity measurements, mineral phases were identified from HighScore Plus software utilizing the Crystallography Open Database (COD; e.g. Grazulis et al. 2009). Silica polymorphs were identified using reference pattern number 96-900-8111 for cristobalite (Dollase 1965), pattern number 96-901-3394 for tridymite (Konnert and Appleman 1978), and pattern number 96-101-1098 for quartz. In sections identified as tridymite-bearing (Whakamaru and Bishop-G), phase proportions were also calculated using an automated Rietveld refinement through HighScore Plus on samples with a crystallinity greater than approximately 75%. Rietveld refinement is utilized to provide a quantification of the variation in tridymite and cristobalite proportions (T/C) throughout the stratigraphic sections. Ellis et al. (2015) identified the tridymite/cristobalite ratio from the Grey's Landing ignimbrite as a qualitative value based on variation in peak height from X-ray diffraction patterns, but we reprocessed their diffraction patterns using the Rietveld refinement to provide a better comparison for this study. The Reitveld refinement does not take into account the amorphous componentry so mineral proportions are recalculated using

AMORPH results (for Whakamaru and Bishop sections) and reported crystallinity values from Ellis et al. (2015) for Grey's Landing.

XRF analyses

Major element compositions were determined from X-ray fluorescence (XRF) at the University of Auckland on a PANalytical Axios 1-kW wavelength dispersive X-ray fluorescence spectrometer (WDXRF) following procedures described in Zorn et al. (2018). Powders for XRF analysis were also used for calculating loss on ignition (LOI) from heating 3.5g of powder for ~ 1hour at 1000 °C.

Density analyses

As defined by Wilson and Hildreth (2003), density provides an analog to welding rank. Densities of coherent (sintered to densely welded) ignimbrite from Whakamaru samples were measured at GNS Science, Wairakei Research Centre, New Zealand. Dry, saturated (wet), and particle densities, as well as apparent porosity, of each sample were measured following the methodology of Hatherton and Leopard (1964). Weighing errors are reported at ± 0.005 g. Two samples were run in duplicate and triplicate with calculated with standard deviation of 0.005 and 0.025 g/cm^3, respectively. Methods used for the Bishop Tuff density samples, are reported in Wilson and Hildreth (2003) and in Supplementary Table 1. No density data are available for the Grey's Landing ignimbrite samples.

RESULTS

Field Observations

Detailed field descriptions for the Bishop are in Wilson and Hildreth (1997), and Andrews and Branney (2011) for the Grey's Landing ignimbrite. Lithologic and stratigraphic

298 descriptions for the Maraetai dam section of the Whakamaru ignimbrite are provided in
299 Martin (1965). Here we describe new exposure characteristics in support of mineralogical
300 observations, with an emphasis on fracture patterns in the Whakamaru ignimbrite. There are
301 distinctive broad differences in fracture patterns throughout the section which are stylistically
302 illustrated in Fig. 2. The lower section (below the dam, corresponding to the Maraetai
303 Ignimbrite of Martin 1965) has visible variations in the dominant orientation of fractures
304 through the section (Fig. 2). The lowest part shows large, columnar, continuous massive units
305 of densely welded ignimbrite (0 to 11m stratigraphic height). A minor horizontal component
306 is present but poorly defined. The dominant fracture spacing at the base of this section is on
307 the order of 1.5 m, with regular smaller scale vertical fractures at an average spacing of 40
308 cm. Up-section, the fracture pattern becomes poorly defined, with neither horizontal nor
309 vertical components dominating. Sampling locations 16MD-2 and -3 show a transitional
310 phase, with irregular sub-vertical and sub-horizontal fractures. From approximately 11 to
311 16m stratigraphic height the dominant fracture pattern follows a well-defined horizontal
312 trend. (Fig. 2B). Spacing between horizontal fractures is between 0.5 -1 m. At sample site
313 16MD-5 semi regular sub-vertical fractures reappear. Horizontal fracturing still dominates at
314 16MD-5 but is progressively lost between 16MD-5 and 16MD-8, with an increasing sub-
315 horizontal to sub-vertical fracture pattern. Sites 16MD-8 to -9 represent the uppermost
316 section of samples from below the dam and correspond to the Maraetai upper flow unit as
317 defined by Martin (1965) (Fig. 2A; Supplemental Figure 1). Large, massive blocks are
318 separated by thin vertical fractures with a minimum of 2 m spacing, suggestive of columnar
319 jointing (Fig. 2C).

320 In the upper section (above the Maraetai dam), the Whakamaru ignimbrite structures
321 are poorly defined and no horizontal jointing component is observed. Massive units are
322 separated by thin fractures spaced 5 to 5.5 m apart. Here, the rock is coherent but non-welded

and decreases in compaction upwards, as evidenced by the shapes of the pumice cavities (increasingly elliptical to circular pumice upwards, compared to unobservable pumice in the lower section). The ignimbrite colour of the upper section (pink) is also distinct from the lower section (grey).

SEM imaging

Representative BSE images from the Whakamaru ignimbrite and Bishop section G are provided in Figs. 4 and 5, respectively. Groundmass textures show evidence of both devitrification (within glass) and vapor phase alteration (within voids) (Fig. 4, 5). The granophyric textures within the glass are most highly developed in sample 16MD-5, with a finer grain size (less mature texture) in samples 16MD-2 and 16MD-9 (Fig. 4). Alkali feldspar has a characteristic axiolitic texture in shards as well as displaying a feathery texture where growing into void space (Fig. 4B,D,H). In the interior of relict glass shards, alkali feldspar and a silica phase (cristobalite or tridymite) are intergrown in a graphic texture (e.g. Fig. 4F). Note, we refer to a silica phase here rather than specifically to cristobalite or tridymite as these are not distinguishable from our BSE images or EDS. Samples 16MD-9 and 16MD-12 have a greater proportion of vapor phase alteration, coincident with the lower apparent compaction compared to samples 16MD-5 and 16MD-2 (Fig. 4). Grain forms in the devitrified texture are predominantly nondescript, with blocky morphologies for silica phases, interspersed with alkali feldspar.

Distinct variations are evident through the Bishop section G samples (Fig. 5). In the lowest part of the section (BR-089), the ignimbrite is densely welded. Although porous, individual glass shards are not easily identifiable. Devitrification of the glassy matrix has resulted in a fine granophyric texture, with streamers of the silica phase interspersed through larger regions of alkali feldspar (Fig. 5F). Although less welded, there is an apparent greater

separation of silica phases and alkali feldspar in sample BR-086, with silica phases elongated, parallel to the length of the glass shards, and surrounded by alkali feldspar (Fig. 5D). A similar but less well developed texture is evident in sample BR-083. Both BR-086 and -083 show evidence for increased vapor-phase alteration: however, like the upper section of the Whakamaru, this is coincident with a decreased density in these samples.

In the Grey's Landing ignimbrite BSE images, all images correspond to the crystalline interior of the ignimbrite, ranging in stratigraphic height from 4 to 48 m (Fig. 6). There is a systematic coarsening of the devitrification texture (alkali feldspar and silica phase), with the development of elongate silica phase minerals, toward the interior of the ignimbrite (Fig. 6B-D). Foliation is also evident in the uppermost ignimbrite samples (e.g. 48 m) with an apparent alignment of iron-oxides (Fig. 6F). Given the lack of porosity and identifiable relict pyroclastic textures, there is no visual evidence of vapor-phase alteration. The Grey's Landing BSE images display a distinctly different texture when compared to both the Bishop and Whakamaru ignimbrite samples (Figs. 4-6). Although a micro-vesicularity is unevenly present through the samples, overall the ignimbrite displays a higher degree of compaction and welding when compared to the Bishop and Whakamaru deposits.

Silica polymorphs

Silica polymorphs (cristobalite, tridymite, quartz), are identified based on X-ray diffraction patterns of ignimbrite samples. Overall, cristobalite and tridymite account for between 25-33% of crystalline phases in all sampled units (Tables 1 and 2; Supplementary Table 2). The proportions of cristobalite and tridymite are negatively correlated, however: as tridymite abundances increase, cristobalite decreases consistently in all three sections where tridymite is observed (Fig. 7). Cristobalite is a significant groundmass component (evidenced by prominent peaks at 21.947° and 36.056° 2Θ; Fig. 8A) in all Whakamaru ignimbrite

samples, averaging 24 ± 5 %. Tridymite, most easily identified by its XRD peak at 20.6° 2Θ, is most abundant within <11 m thickness of the stratigraphic section, primarily in samples 16MD-3b (15 m section height) to 16MD-5b (21 m section height) varying from 1.5 to 15 %, with lesser proportions of 1.2 % in 16MD-7 (31 m section height) and <1% above 16MD-8 (41 m section height). Low abundances of tridymite (less than ~1%) are unresolvable based on appearance of distinct diffraction peaks and are only identified from Rietveld refinement. The tridymite/cristobalite (T/C) ratio varies significantly over this stratigraphic range, with a maximum relative T/C ratio of 1.3 at 18 m height (Fig. 9).

Bishop Tuff sections B, G, and H (Fig. 1) each have substantial differences in their silica polymorphs. Quartz, which occurs in all the Bishop samples as a major phenocryst component, is commonly observed in varying proportions in the diffraction patterns, likely representing microphenocrysts in the groundmass (Hildreth, 1979). Quantified during Rietveld refinement, in section G quartz concentrations vary from 0.3-1.5%. In section B, all samples with <20% groundmass crystallinity lack XRD evidence of either cristobalite or tridymite (Fig. 8D). The 100%I (21.947° 2Θ) cristobalite peak overlaps with phenocryst phase Na-rich plagioclase feldspar (e.g. oligoclase; Hildreth, 1979) and the cristobalite 14%I peak at 36.056° 2Θ is notably missing in these cases (Fig. 8D, samples BR159-B and BR145-B). Thus, the diffraction peak at 21.7° 2Θ is most likely associated with Na-rich plagioclase feldspar.

Excluding the upper vitrophyre, all analysed samples from section H contain significant amounts of cristobalite, and tridymite is notably absent. In section G, cristobalite is present in all samples, however unlike in section H, tridymite is also evident in samples BR-085 to -087, from 74 to 77 m in the section (Fig. 9; Wilson and Hildreth 2003). Cristobalite concentrations in section G are relatively constant (30 ± 2%) in samples where tridymite is absent, but decrease to ~15% as tridymite proportions increase (Fig. 8). The T/C

ratio reaches a maximum of 1.0 from 74 to 76 m stratigraphic height then decreases rapidly up section. A large gap in available samples in the stratigraphic section from 56 to 74 m precludes an assessment of the symmetry of the T/C ratio in this section, especially given the relatively narrow range over which the ratio decreases up section (Fig. 9).

Cristobalite is ubiquitous in Grey's Landing samples (excluding upper and lower vitrophyre), with concentrations varying from ~10-30%. Tridymite is observed through most of the stratigraphic sequence, from 8-36 m stratigraphic height and varies from 0 to 20%, resulting in a T/C ratio of 0 to 1.9 (Fig. 9). Tridymite is more widespread and its proportions greater than observed in either the Whakamaru or Bishop section G.

Crystallinity

Crystallinity measurements from the Whakamaru (Maraetai dam section) ignimbrite predominantly record highly crystalline conditions. Both whole rock and separated fines have crystallinities almost exclusively >90% (Supplemental Table 3). Whole rock crystallinities remain above 95% except in the uppermost ~10 m of samples (16MD-WR-11 to 16MD-WR-14), consistent with less welding and compaction from field observations in those samples (Fig. 4, 9). Groundmass crystallinity is up to 15% lower than whole rock crystallinity, ranging from 71 to 94% and generally decreasing up section. Full crystallinity results processed through AMORPH are available in Supplemental Table 3 and summarized for groundmass analyses in Table 1.

Only groundmass crystallinity was measured from the Bishop sections (G, H, B; Figs. 9, 10). Section B is primarily glassy, with crystallinities varying from 3-44%, with only 30% of the analyzed samples having groundmass crystallinities >20%. Sections G and H have crystallinities more similar to the Whakamaru section. Section H ranges from 59-94%,

422 excluding an upper vitrophyre with 3% groundmass crystallinity, while Section G
423 groundmass crystallinity varies from 75 to 93% (Tables 1 and 2).

424 Whole rock and groundmass crystallinity of the Grey's Landing ignimbrite samples
425 are reported in Ellis et al. (2015). Within the crystalline core of the ignimbrite, groundmass
426 crystallinities vary from 76 to 93%, while glassy vitrophyre ranges only from 4 to 16%,
427 creating a bimodal crystallinity distribution (Table 1). There is no systematic variation in
428 groundmass crystallinity through the crystalline core of the ignimbrite, and transitions
429 between the core and the vitrophyre are sharp.

430

431 **Major element composition**

432 Major element compositions for the Whakamaru ignimbrite show no systematic
433 variation along its stratigraphy (Table 3). LOI values are generally <1 wt% (excluding an
434 outlier value of 2.1 wt% in sample 16MD-6) between samples 16MD-1 and 16MD-8.
435 Upwards, in samples 16MD-9 to 16MD-14, LOI values increase to a maximum of 3.4 wt%.

436

437 **Density and Porosity**

438 Density measurements of the Whakamaru ignimbrite samples vary from 2.16 to 1.53
439 g/cm^3 (Table 1; Supplemental Table 4). Similar bulk densities for samples 16MD-1 to
440 16MD-7 yield an average of 2.11 ± 0.03 g/cm^3. Stratigraphically above sample 16MD-7
441 densities decrease to the break in section with 16MD-9 at 1.80 g/cm^3. In the upper
442 Whakamaru section, densities vary from 1.53 to 1.66 g/cm^3. Apparent porosities are
443 negatively and linearly correlated to density, ranging from 17 to 39.3% (Supplemental Table
444 4). Porosities are constant from 15 to 20% in the lowermost samples (16MD-1 to 16MD-7),
445 increasing to 30% to the top of the lower section (below the dam), and then consistently

range from 35-39% in the upper section (above the dam). Henceforth, we utilize only density values from the Whakamaru ignimbrite to provide a direct correlation to the Bishop samples.

Densities for Bishop samples are variable through the sections with a total range from 1.22 to 2.34 g/cm^3 (Tables 1 and 2; Wilson and Hildreth 2003), where sections G and H have similar density profiles, with densities >2 g/cm^3 near the base of the section then density minima above the contact between ignimbrite Ig1Eb and Ig2Eb, and at the top of Ig2Eb (Figs. 9 and 10)10. Clast densities for section B are initially low (<1.8 g/cm^3), increase across the contact between Ig1Ea and Ig1Eb (and inter-bedded fall deposit), reach a maximum of 2.07 g/cm^3 and then decrease to the top of the section (Fig. 10).

DISCUSSION

Tridymite and cristobalite in ignimbrites

Both tridymite and cristobalite are present in all three ignimbrite sections: however, the relative distribution is different between the Whakamaru, Bishop, and Grey's Landing ignimbrite. In welded materials, cristobalite is the dominant silica polymorph, ubiquitous in the Whakamaru and Grey's Landing ignimbrite samples and common in sections G and H of the Bishop, while tridymite is relatively rare. It is the scarcity of tridymite in these cases that provides an opportunity to refine models of deposition, cooling, and crystallization. In the following discussion, endmember examples of the distribution of tridymite relative to other ignimbrite properties are detailed using the Bishop and Grey's Landing ignimbrite sections. This is followed by discussion of the distribution of tridymite in the less-constrained stratigraphic context of the Whakamaru ignimbrite.

The occurrence of tridymite in the Bishop ignimbrite (section G) is over a very narrow region (~3 m) and corresponds to the contact between ignimbrites Ig1Eb and Ig2Eb (Fig. 9; Wilson and Hildreth 2003). However, the rock density decreases consistently over

this lithologic contact and the actual density minimum is located above/outside of the tridymite zone (Fig. 9). Notably in Bishop section G, a decrease of ~10 vol% groundmass crystallinity corresponds to the lithologic contact between ignimbrite packages (uncorrelated to sample density: Fig. 9). Despite the change in groundmass crystallinity over the tridymite zone, there is no correlation between the T/C ratio, or tridymite abundance, to the groundmass crystallinity or density. This suggests that the important variable here in regulating the appearance and proportion of tridymite is not the groundmass crystallinity or density, but the presence of lithologic contacts between ignimbrite emplacement packages.

The other Bishop sections (B, H) portray a range of different features which allow us to evaluate the occurrence of tridymite in section (G). Bishop section H has almost an identical density and groundmass crystallinity profile to Bishop section G (Figs. 9 and 10). In addition, field evidence indicates a wide zone of vapor-phase alteration in Ig2Eb above the fall horizon in section H (Wilson and Hildreth 2003). However, importantly, there is no tridymite observed in section H, despite the field evidence for vapor-phase alteration. The only significant variation in these two sections is structural; section H contains ~5 m of ignimbrite Ig2Ea and parts of fall units F8 and F9 sandwiched between the more massive Ig1Eb and Ig2Eb ignimbrite packages (Fig. 10). This would suggest that the presence of the fall units (and minor ignimbrite) reflects an altered cooling and degassing history, inhibiting the formation of tridymite at the lithologic contact in this section.

Bishop section B has markedly different density and crystallinity profiles to sections G and H. Densities (<2 g/cm^3) and groundmass crystallinities (<40 vol %) are generally lower. However, these parameters are positively correlated, largely driven by differences in density and crystallinity between the two ignimbrite packages (Ig1Ea and Ig1Eb), with higher densities and groundmass crystallinities observed in Ig1Eb compared to the glassy Ig1Ea unit. Because of the overall low crystallinity in both units, it is impossible to accurately

distinguish the cristobalite and feldspar peaks from the XRD results. However, no lower intensity cristobalite peaks are evident at higher 2θ in the X-ray patterns. Similarly, no tridymite is identified in any of the section B samples. These results support limited vapor-phase alteration or devitrification, and only in higher density samples in Ig1Eb.

The single, densely welded rheomorphic Grey's Landing ignimbrite provides a distinctive contrast to the multiple flow packages and fall deposits of the Bishop Tuff. In contrast to the Bishop sections, tridymite is present in ~60% of the 45 m thick crystalline core of the ignimbrite. The abundances of tridymite (and T/C ratios) are not symmetrical through the ignimbrite but rather are skewed toward the lower half of the deposit (Fig. 9). While this matches numerical models of cooling profiles (Ellis et al. 2015), it clearly does not take into account the relative movement of these phase transitions as a result of compaction in the rheomorphic ignimbrite. Interestingly, the coarsest groundmass textures (Fig. 6) do not correlate to the highest proportion of tridymite in the groundmass (Fig. 9), suggesting that the proportion of tridymite is not simply a function of cooling rate.

In the Whakamaru ignimbrite, tridymite is observed roughly two-thirds of the way up section (from the base; Fig. 11; Supplemental Figure 1). The two competing possible interpretations of flow packages and welding in this section affect the consideration of tridymite growth in relation to ignimbrite emplacement (Martin 1965; Briggs 1976b). XRF analyses are inconclusive in differentiating potential flow packages, and LOI measurements, with one exception, are all low (less than 1 wt%; Table 3) through the lower ~57 m of the section, gradually increasing upwards into the upper Whakamaru ignimbrite. As the tridymite zone corresponds to the horizontal jointing, this therefore implies that the tridymite zone may occur at a contact between flow packages (Martin 1965) or approximately midway through subunit D (Briggs 1976b; Brown et al. 1998), the former paralleling the distribution in the Bishop Tuff and the latter more consistent with the distribution in the Grey's Landing

ignimbrite. However, as Whakamaru subunits A-E (Briggs 1976b) have been proposed to represent a single cooling unit, the distribution of tridymite within the cooling unit as a whole is inconsistent with the Grey's Landing ignimbrite crystallization pattern. Regardless of the structural model, however, we note the key observation is the correlation between the horizontal/sub-horizontal fracture patterns and the emergence of the tridymite zone (Figs. 9 and 11).

The change in fracture pattern also corresponds to irregular variations in groundmass crystallinity, varying from 90% to 100%. Tridymite occurrences up-section are predominantly in samples from the sub-horizontal to horizontal fracture pattern zones (16MD-3b) but extend up through the transition zone until fractures return to a sub-vertical predominant pattern (16MD-7; Fig. 2). Although the maximum T/C ratio is observed within the zone dominated by pervasive horizontal fractures, these ratios slowly decrease up through overlying ignimbrite (Fig. 9). Density values show no obvious correlation to the appearance of tridymite and are constant (~2.1 g/cm^3) through the tridymite-bearing zone. Similarly, despite the variations in groundmass crystallinity over this critical zone (~10 vol%), there is no clear correlation to the proportion or occurrence of tridymite (Fig. 9). However, despite textural complexities evident in BSE imaging, we do note that the tridymite zone corresponds to a coarser-grained devitrification texture (Figs. 4E-F and 5C-D). Field observations, textures, crystallinity and density measurements all indicate that localized processes, such as gas pressure or permeability, control the distribution of tridymite in the ignimbrites.

Mechanisms of tridymite formation

The stability or metastability of tridymite is largely a function of temperature and the availability of alkali oxides and water (e.g. Fenner 1913; Garofalini and Miller 1986; Stevens et al. 1997). In the following discussion we first examine the potential formation of higher-

546 temperature stable tridymite in the Grey's Landing section, and then examine lower-
547 temperature metastable tridymite formation in both the Bishop and Whakamaru sections.
548 Assuming availability of alkalis, at magma temperatures suggested by Fe-Ti oxides
549 for the studied ignimbrites (Brown et al. 1998; Hildreth and Wilson 2007; Andrews et al.
550 2008; Matthews et al. 2012), only the Grey's Landing ignimbrite (>900 °C) has the potential
551 to form stable β-tridymite (e.g. Fenner 1913). Ellis et al. (2015) suggest that tridymite
552 occurrences in the rheomorphic Grey's Landing ignimbrite correlate to cooling rates of the
553 ignimbrite. However, this depends on the mechanism of tridymite formation. As discussed
554 above, the densely welded texture with minimal micro-porosity of the Grey's Landing
555 ignimbrite (Fig. 4) favors the formation of silica polymorphs through devitrification as
556 opposed to pervasive vapor-phase alteration. If stable β-tridymite is forming during
557 devitrification, this must occur rapidly after emplacement, before temperatures drop below
558 ~870 °C. Andrews and Branney (2011) suggest textures indicate cooling through the solidus
559 before reaching a calculated glass transition temperature of ~725 to 525 °C (from dry to 1
560 wt% H_2O, respectively). A maximum cooling time (slowest cooling rate) from numerical
561 modelling suggests the Grey's Landing ignimbrite interior would reach temperatures below
562 ~870 °C after approximately 2.5 years (Ellis et al. 2015), after which quartz would constitute
563 the stable silica polymorph. However, thermal heterogeneities, vertical fracturing, and any
564 influx of meteoric or surface water all will decrease this cooling time (e.g. Keating 2005;
565 Randolph-Flagg et al. 2017). The presence of cristobalite, and lack of tridymite, at the top
566 and bottom of the Grey's Landing ignimbrite section is explained by results from
567 crystallization experiments, which demonstrate cristobalite is formed as a metastable phase in
568 the cooling-related phase transitions from amorphous volcanic glass (silica-rich) to tridymite
569 (Wu et al. 2002).

570 Similar observations of "magmatic" or primary tridymite were suggested for high-
571 temperature rheomorphic ignimbrites and rhyolitic lavas from the Keweenawan Midcontinent
572 Rift (USA: Green and Fitz 1993) and the Harvey volcanics (New Brunswick, Canada: Payette
573 and Martin 1986). Rowe et al. (2012) also recognized high proportions of tridymite
574 throughout the Tuff of Knob, another high-temperature SR-type ignimbrite. They suggested
575 however that, based on the presence of quartz as well, the tridymite was metastable. The
576 limited presence of quartz may also be explained by the slow kinetics associated with
577 structural changes from tridymite to quartz (e.g. Gibbs 1926).
578 Alternatively, if devitrification is a slower process, occurring after significant cooling,
579 then tridymite would likely form as a metastable phase (<870 °C). At this point, the transition
580 from metastable cristobalite to tridymite would reflect the longer duration of cooling.
581 Although both metastable phases will nucleate together, their relative proportion will change
582 from cristobalite-dominant to tridymite-dominant, resulting from the faster initial
583 crystallization rate of cristobalite, followed by its transformation to tridymite (Madden and
584 Van Vlack 1967; Garofilini and Miller 1986; Wu et al. 2002).
585 Tridymite is commonly associated with vapor phase alteration (Caporuscio et al.
586 2012) or extending cooling times beneath the glass transition temperature (Ellis et al. 2015).
587 BSE images from both the Bishop section G and Whakamaru ignimbrite samples suggest a
588 combination of devitrification and vapor-phase alteration accompanied tridymite growth
589 (Figs. 4 and 5). As discussed above, regardless of the mechanism of formation, due to the
590 lower temperatures of the Bishop Tuff and Whakamaru ignimbrite tridymite will be
591 metastable.
592 In the Bishop Tuff section G, there is no significant change in crystallinity in the
593 tridymite zone compared to the ignimbrite above or below it (Fig. 4), indicating that the
594 appearance of tridymite does not appreciably increase the overall groundmass crystallinity.

595 Importantly, as the proportion of tridymite increases, we see a corresponding linear decrease
596 (with a slope of -1) in the proportion of cristobalite (Fig. 7). This change in relative
597 proportions of silica polymorphs, without a corresponding change in groundmass
598 crystallinity, suggests a phase transition from cristobalite to tridymite. We see a similar
599 correlation in the Whakamaru section, where samples 16MD-2 and 16MD-3 both have
600 groundmass crystallinities greater than 90%, greater than or comparable to the groundmass
601 crystallinity in the tridymite zone (Fig. 9). Despite this, we see the same negative correlation
602 between tridymite and cristobalite correlation suggesting the tridymite formation comes at the
603 expense of cristobalite (Fig. 7B).

604 Within the Bishop, the localization of tridymite to the direct contact between Ig1Eb
605 and Ig2Eb implies a structural characteristic of the ignimbrite or its emplacement history
606 around this contact is what regulates the presence of tridymite. A model describing thermal
607 and gas pressure fluctuations for two 50 m thick ignimbrites (emplaced 20 days apart in this
608 model) suggest that for at least the first two months, the maximum gas pressure will coincide
609 with the lithologic contact, but that the pressure rapidly decreases after emplacement (Riehle
610 2015). In contrast, results of the thermal model suggests that the maximum temperature after
611 up to 4 years is at the lithologic contact between ignimbrites (Riehle 2015). However, neither
612 of these two models is appropriate for the Bishop Tuff because of the evidence for rapid
613 emplacement of the flow packages together with their coeval fall deposits (Wilson and
614 Hildreth 2003). As discussed above, the primary difference in sections G and H is the
615 presence of fall deposits and ignimbrite making an approximate 5 m-thick high porosity
616 transition between denser welded ignimbrite packages. We propose that the upper denser-
617 welded tuff (Ig2Eb) served as a sealant for gas escape from the lower ignimbrite but that the
618 interbedded fall deposits in section H served as a permeable, laterally continuous bed to keep
619 vapor pressure reduced. Thus in contrast, high gas pressure near the Bishop flow package

620 contact in section G facilitated tridymite precipitation while high temperatures promote
621 increased devitrification (Keating 2005). Despite the origin of the horizontal fractures in the
622 Whakamaru, corresponding to either a change in welding (Briggs 1976a,b) or a flow package
623 contact (Martin 1965) we propose that this change in jointing with overlying thick ignimbrite
624 served to restrict gas escape in a similar fashion as observed in the Bishop G section (Fig.
625 11).

626 An alternative model to explain tridymite crystallization along the flow package
627 boundaries is through post-depositional hydrothermal circulation, where geothermal fluids
628 utilize laterally continuous zones of higher permeability (Bignall et al. 2010). However,
629 vapor-phase mineral growth and devitrification are the only textures evident related to
630 secondary mineralization (Figs. 4 and 5). There is no evidence for more widespread
631 silicification, a change in major element composition, or a change in density/porosity
632 associated with tridymite deposition compared to cristobalite-only samples (Fig. 9).
633 Similarly, since tridymite appears to form directly at the expense of cristobalite, our
634 observations are unlikely to relate to a separate hydrothermal alteration event (Fig. 7B).
635 Lastly, there is no evidence of low temperature hydrolysis reactions in the form of secondary
636 hydrous phases such as clays (Fig. 8). All of these factors point to tridymite formation
637 associated with initial cooling and degassing of the ignimbrites. Thus, we predict that
638 tridymite, formed predominantly through vapor-phase alteration, serves as a potential
639 fingerprint for horizontal structures or lithologic contacts with initial higher porosities,
640 capable of localizing prolonged crystallization prior to compaction to the modern state.
641

642 **IMPLICATIONS**

643 The occurrence and distribution of tridymite in the Grey's Landing, Bishop, and
644 Whakamaru large silicic ignimbrites are highly variable. Unlike the widespread distribution

of cristobalite in volcanic rocks, our results imply that tridymite crystallization is dependent on emplacement temperature and localized conditions promoting trapping of gas phases and slow cooling.

At one extreme, high temperature ignimbrites (>870 °C) such as Grey's Landing have the potential to preserve stable tridymite, crystallizing rapidly under high temperature conditions shortly after emplacement. In these instances, tridymite abundances and T/C ratios, in conjunction with geothermometry and groundmass textures, may preserve an ignimbrite thermal history, with the variations in T/C ratios recording a cooling profile. Coupled with numerical thermal models or chronometers (Ellis et al. 2015, 2018), T/C variations have the potential to inform maximum timescales of devitrification.

Under lower temperature conditions (<870 °C) tridymite exists as a metastable phase. The occurrence of tridymite in the welded Whakamaru and Bishop (section G) ignimbrites, is limited to interpreted lithologic boundaries, in particular, contacts between flow packages. We propose that: 1), upper denser-welded material serve as seals, trapping degassing volatiles from lower flow packages, and 2) contacts initially serve as short-lived permeable zones, preserving conditions for tridymite vapor-phase crystallization, whereas the lower permeability of the upper material must inhibit vapor-phase tridymite formation. In ignimbrites either lacking a seal (Bishop section B), or in the case of Bishop section H, containing an interbedded and highly permeable fall deposit, gas pressures are not maintained to promote tridymite formation. These results imply a new methodology for assessing syn- and post-emplacement petrogenetic processes in an important but relatively minor mineralogical component.

One outgrowth of this study arises from the observation that welded ignimbrites are the dominant rock type in numerous geothermal reservoirs associated with silicic volcanic systems (e.g. Taupo Volcanic Zone, New Zealand; Coso Hot Springs, U.S.A.; Kyushu

Japan). Beyond volcanological implications, one of the initial drivers of this research was to understand if there exists a relationship between changing fracture patterns and groundmass mineralogy that could improve understanding of fluid flow in the Whakamaru ignimbrite where it forms a geothermal reservoir rock (e.g. Milicich et al. 2018). Laterally continuous permeable zones both within and between ignimbrite formations are recognized as important controls of fluid flow (Bignall et al. 2010). However, Milicich et al. (2018) highlight the challenge of identifying stratigraphic sequences from drill cuttings in geothermal wells. Our results from moderate-temperature welded ignimbrites (Bishop and Whakamaru) suggest that tridymite is localized to contacts between pyroclastic flow packages. At least in the case of the Whakamaru section at Maraetai, we see that this contact coincides with a distinctive reorientation of dominant fracture patterns to horizontal, and thus the potential for localized changes to permeability and fluid flow regimes in a reservoir host stratigraphy (Fig. 2). While further testing on geothermal well cuttings is required, tridymite may prove to be a useful mineralogical tracer of depositional contacts in silicic geothermal reservoirs.

ACKNOWLEDGEMENTS

We thank the technical staff at the University of Auckland (UoA) and the UoA X-ray Center for access to facilities, and Dawid Szymanowski for preparation of Whakamaru thin sections. Partial financial support was provided by GNS Science (C05X1702: Strategic Science Investment Fund, New Zealand's Geothermal Future) and UoA School of Environment PBRF funding (awarded to Rowe 2017/2018).

REFERENCES

694 Andrews G.D.M., and Branney, M.J. (2011) Emplacement and rheomorphic deformation of a
695 large, lava-like rhyolitic ignimbrite: Grey's Landing, southern Idaho. Geological Society of
696 America Bulletin, 123, 725-743.

697 Andrews, G.D.M., Branney, M.J. Bonnichsen, B., and McCurry, M. (2008) Rhyolitic
698 ignimbrites in the Rogerson Graben, southern Snake River Plain volcanic province: volcanic
699 stratigraphy, eruption history and basin evolution. Bulletin of Volcanology, 70, 269-291.

700 Branney, M.J., Bonnichsen, B., Andrews, G.D.M., Ellis, B., Barry, T.L., and McCurry, M.
701 (2008) 'Snake River (SR)-type' volcanism at the Yellowstone hotspot track: distinctive
702 products from unusual high-temperature silicic super-eruptions. Bulletin of Volcanology, 70,
703 293-314.

704 Briggs, N.D. (1976a) Welding and crystallization zonation in Whakamaru Ignimbrite, central
705 North Island, New Zealand. New Zealand Journal of Geology and Geophysics, 19, 189-212.

706 Briggs, N.D. (1976b) Recognition and correlation of subdivisions within the Whakamaru
707 Ignimbrite, central North Island, New Zealand. New Zealand Journal of Geology and
708 Geophysics, 19, 463-501.

709 Bignall, G., Milicich, S., Ramirez, E., Rosenberg, M., Kilgour, G., and Rae, A. (2010)
710 Geology of the Wairakei-Tauhara geothermal system, New Zealand. Proceedings, World
711 Geothermal Congress, Bali, Indonesia, 25-29 April 2010.

712 Brown, S.J.A., Wilson, C.J.N., Cole, J.W., and Wooden, J. (1998) The Whakamaru group
713 ignimbrites, Taupo Volcanic Zone, New Zealand: evidence for reverse tapping of a zoned
714 silicic magmatic system. Journal of Volcanology and Geothermal Research, 84, 1-37.

715 Caporuscio, F.A., Gardner, J.N., Schultz-Fellenz, E.S., and Kelley, R.E. (2012) Fumarolic
716 pipes in the Tshirege member of the Bandelier Tuff on the Pajarito Plateau, Jemez
717 Mountains, New Mexico. Bulletin of Volcanology, 74, 1023-1037.

718 Cavazos-Álvarez, J.A., Carrasco-Núñez, G., Dávila-Harris, P., Peña, D., Jáquez, A. and
719 Arteaga, D. (2020) Facies variations and permeability of ignimbrites in active geothermal
720 systems; case study of the Xáltipan ignimbrite at Los Humeros Volcanic Complex. Journal of
721 South American Earth Sciences, 104, 102810.

722 Dollase, W.A. (1965) Reinvestigation of the structure of low cristobalite. Zeitschrift für
723 Kristallographie, 121, 369-377.

724 Downs, D.T., Wilson, C.J.N., Cole, J.W., Rowland, J.V., Calvert, A.T., and Leonard, G.S.
725 (2014) Age and eruptive center of the Paeroa Subgroup ignimbrites (Whakamaru Group)
726 within the Taupo Volcanic Zone of New Zealand. Geological Society of America Bulletin,
727 126, 1131-1144.

728 Ellis, B.S., Barry, T., Branney, M.J., Wolff, J.A., Bindeman, I., Wilson, R., and Bonnichsen,
729 B. (2010) Petrologic constraints on the development of a large-volume, high temperature,
730 silicic magma system: The Twin Falls eruptive centre, central Snake River Plain. Lithos, 120,
731 475-489.

732 Ellis, B.S., Cordonnier, B., Rowe, M.C., Szymanowski, D., Bachmann, O., and Andrews,
733 G.D.M. (2015) Groundmass crystallization and cooling rates of lava-like ignimbrites: the
734 Grey's landing ignimbrite, southern Idaho, USA. Bulletin of Volcanology, 77, 87.

735 Ellis, B.S., Szymanowski, D., Magna, T, Neukampf, J., Dohmen, R., Bachmann, O, Ulmer,
736 P., and Guillong, M. (2018) Post-eruptive mobility of lithium in volcanic rocks. Nature
737 Communications, 9, 3228.

738 Ewart, A. (1965) Mineralogy and petrogenesis of the Whakamaru ignimbrite in the Maraetai
739 area of the Taupo volcanic zone, New Zealand. New Zealand Journal of Geology and
740 Geophysics, 8, 611-677.

741 Fenner, C.N. (1913) The stability relations of silica minerals. American Journal of Science,
742 series 4, 36, 331-384.

743 Flörke, O.W., and Langer, K. (1972) Hydrothermal recrystallization and transformation of
744 tridymite. Contributions to Mineralogy and Petrology, 46, 221-230.

745 Froggatt, P.C., Nelson, C.S., Carter, L., Griggs, G., and Black, K.P. (1986) An exceptionally
746 large late Quaternary eruption from New Zealand. Nature, 319, 578-582.

747 Garofalini, S.H., and Miller, A.D. (1986) Kinetics of tridymite formation. Journal of Crystal
748 Growth, 78, 85-96.

749 Gibbs, R.E. (1926) The polymorphism of silicon dioxide and the structure of tridymite.
750 Proceedings of the Royal Society of London, series A, 113, 351-368.

751 Grazulis, S., Chateigner, D., Downs, R.T., Yokochi, A.T., Quiros, M., Lutterotti, L.,
752 Manakova, E., Butkus, J., Moeck, P., and Le Bail, A. (2009) Crystallography Open Database
753 – an open-access collection of crystal structures. Journal of Applied Crystallography, 42,
754 726-729.

755 Green, J.C., and Fitz III, T.J. (1993) Extensive felsic lavas and rheoignimbrites in the
756 Keweenawan Midcontinent Rift plateau volcanics, Minnesota: petrographic and field
757 recognition. Journal of Volcanology and Geothermal Research, 54, 177-196.

758 Grunder, A., and Russell, J.K. (2005) Welding processes in volcanology: insights from field,
759 experimental, and modeling studies. Journal of Volcanology and Geothermal Research, 142,
760 1-9.

761 Hatherton, T., and Leopard, A.E. (1964) The densities of New Zealand rocks. New Zealand
762 Journal of Geology and Geophysics, 7, 605-625.

763 Hildreth, W. (1979) The Bishop Tuff: evidence for the origin of compositional zonation in
764 silicic magma chambers. In C.E. Chapin and W.E. Elston, Eds., Ash-Flow Tuffs. Geological
765 Society of America Special Papers, 180, 43-79.

766 Hildreth, W. (2004) Volcanological perspectives on Long Valley, Mammoth Mountain, and
767 Mono Craters: several contiguous but discrete systems. Journal of Volcanology and
768 Geothermal Research, 136, 169-198.

769 Hildreth, W., and Fierstein, J. (2017) Geologic field-trip guide to Long Valley Caldera,
770 California. U.S. Geological Survey Scientific Investigations Report, 2017–5022–L, 119 p.

771 Hildreth, W., and Wilson, C.J.N. (2007) Compositional zoning of the Bishop Tuff. Journal of
772 Petrology, 48, 951-999.

773 Holmquist, S.B. (1961) Conversion of quartz to tridymite. Journal of the American Ceramic
774 Society, 44, 82-86.

775 Jones, J.B., and Segnit, E.R. (1972) Genesis of cristobalite and tridymite at low temperatures.
776 Journal of the Geological Society of Australia, 18, 419-422.

777 Keating, G.N. (2005) The role of water in cooling ignimbrites. Journal of Volcanology and
778 Geothermal Research, 142, 145-171.

779 Keith, T.E.C. (1991) Fossil and active fumaroles in the 1912 eruptive deposits, Valley of Ten
780 Thousand Smokes, Alaska. Journal of Volcanology and Geothermal Research, 45, 227-254.

781 Knott, T.R., Branney, M.J., Reichow, M.K., Finn, D.R., Tapster, S. and Coe, R.S. (2020)
782 Discovery of two new super-eruptions from the Yellowstone hotspot track (USA): Is the
783 Yellowstone hotspot waning? Geology, 48, 934-938.

784 Konnert, J.H., and Appleman, D.E. (1978) The crystal structure of low tridymite. Acta
785 Crystallographica, Section B, 34, 391-403.

Lofgren, G. (1971) Experimentally produced devitrification textures in natural rhyolitic glass. Geological Society of America Bulletin, 82, 111-124.

Madden, G.I., and Van Vlack, L. (1967) Transformation of quartz to tridymite in the presence of binary silicate liquids. Journal of the American Ceramic Society, 50, 414-418.

Martin, R.C. (1965) Lithology and eruptive history of the Whakamaru Ignimbrites in the Maraetai area of the Taupo Volcanic Zone, New Zealand. New Zealand Journal of Geology and Geophysics, 8, 680-701.

Matthews, N.E., Smith, V.C., Costa, A., Durant, A.J., Pyle, D.M., and Pearce, N.J.G. (2012) Ultra-distal tephra deposits from super-eruptions: examples from Toba, Indonesia and Taupo Volcanic Zone, New Zealand. Quaternary International, 258, 54-79.

McClelland, E., Wilson, C.J.N., and Bardot, L. (2004) Palaeotemperature determinations for the 1.8-ka Taupo ignimbrite, New Zealand, and implications for the emplacement history of a high-velocity pyroclastic flow. Bulletin of Volcanology, 66, 492-513.

Milicich, S.D., Massiot, C., McNamara, D.D. (2018) Volcanic texture identification and influence on permeability using a borehole resistivity image log in the Whakamaru Group ignimbrite, Wairakei Geothermal Field, New Zealand. Proceedings, 43rd Workshop on Geothermal Reservoir Engineering Stanford University, Stanford, California, February 12-14, 2018 SGP-TR-213.

Payette, C., and Martin R.F. (1986) The Harvey volcanic suite, New Brunswick. II. Postmagmatic adjustments in the mineralogy and bulk composition of a high-fluorine rhyolite. Canadian Mineralogist, 24, 571-584.

Randolph-Flagg, N., Breen, S., Hernandez, A., Manga, M., and Self, S. (2017) Evenly spaced columns in the Bishop Tuff (California, USA) as relicts of hydrothermal cooling. Geology, 45, 1015-1018.

Riehle, J.R. (2015) Relations between thermal history and secondary structures of ignimbrites exclusive of rheomorphism. Geosphere, 11, 572-605.

Ross, C.S., and Smith, R.L. (1961) Ash-flow tuffs: their origin, geologic relations and identification. U.S. Geological Survey Professional Paper, 366, 1-81.

Rowe, M.C., and Brewer, B. (2018) AMORPH: A statistical program for characterizing amorphous materials by X-ray diffraction. Computers and Geosciences, 120, 21-31.

Rowe, M.C., Ellis, B.S., and Lindeberg, A. (2012) Quantifying crystallization and devitrification of rhyolites by means of X-ray diffraction and electron microprobe analysis. American Mineralogist, 97, 1685-1699.

Schipper, I.C., Rickard, W.D.A., Reddy, S.M., Saxey, D.W., Castro, J.M., Fougerouse, D., Quadir, Z., Conway, C., Prior, D.J., and Lilly, K. (2020) Volcanic SiO_2-cristobalite: a natural product of chemical vapor deposition. American Mineralogist, 105, 510-524.

Quane, S.L., and Russell, J.K. (2005). Ranking welding intensity in pyroclastic deposits. Bulletin of Volcanology, 67, 129-143.

Sheridan, M.F. (1970) Fumarolic mounds and ridges of the Bishop Tuff, California. Geological Society of America Bulletin, 81, 851-868.

Smith, R.L. (1960a) Zones and zonal variations in welded ash flows. U.S. Geological Survey Professional Paper, 354-F, 147-159.

Smith, R.L. (1960b) Ash flows. Geological Society of America Bulletin, 71, 795-842.

Spycher, N.F., Sonnenthal, E.L., and Apps, J.A. (2003) Fluid flow and reactive transport around potential nuclear waste emplacement tunnels at Yucca Mountain, Nevada. Journal of Contaminant Hydrology, 62, 653-673.

832 Stevens, S.J., Hand, R.J., and Sharp, J.H. (1997) Polymorphism of silica. Journal of Materials
833 Science, 32, 2929-2935.

834 Streck, M.J., and Grunder, A.L. (1995) Crystallization and welding variations in a
835 widespread ignimbrite sheet; the Rattlesnake Tuff, eastern Oregon, USA. Bulletin of
836 Volcanology, 57, 151-169.

837 Wilson, C.J.N., and Hildreth, W. (1997) The Bishop Tuff: new insights from eruptive
838 stratigraphy. Journal of Geology, 105, 407-439.

839 Wilson, C.J.N., and Hildreth, W. (2003) Assembling an ignimbrite: mechanical and thermal
840 building blocks in the Bishop Tuff, California. Journal of Geology, 111, 653-670.

841 Wilson, C.J.N., Houghton, B.F., and Lloyd, E.F. (1986) Volcanic history and evolution of the
842 Maroa-Taupo area, central North Island. In I.E.M. Smith, Ed., Late Cenozoic Volcanism in
843 New Zealand. Royal Society of New Zealand Bulletin, 23, 194-223.

844 Wright, H.M., and Cashman, K. (2014) Compaction and gas loss in welded pyroclastic
845 deposits as revealed by porosity, permeability and electrical conductivity measurements of
846 the Shevlin Park Tuff. Geological Society of America Bulletin, 126, 234-247.

847 Wright, H.M., Lesti, C., Cas, R.A.F., Porreca, M., Viramonte, J.G., Folkes, C.B., and
848 Giordano, G. (2011) Columnar jointing in vapor-phase-altered, non-welded Cerro Galan
849 Ignimbrite, Paycuqui, Argentina. Bulleting of Volcanology, 73, 1567-1582.

850 Wu, S.-W., Wong, D.S.H., and Lu, S.-Y. (2002) Size effects on silica polymorphism. Journal
851 of the American Ceramic Society, 85, 2590-2592.

852 Zorn, E.U., Rowe, M.C., Cronin, S.J., Ryan, A.G., Kennedy, L.A., and Russell, J.K. (2018)
853 Influence of porosity and groundmass crystallinity on dome rock strength: a case study from
854 Mt. Taranaki, New Zealand. Bulletin of Volcanology, 80, 35.

855

856 FIGURE CAPTIONS

857 Figure 1: Location maps of (A) Maraetai Dam locality of the Whakamaru ignimbrite, New
858 Zealand; (B) Owens Gorge sections B, G, and H of the Bishop ignimbrite from Wilson and
859 Hildreth (2003); and (C) the Backwaters section of the Grey's Landing ignimbrite, central
860 Snake River Plain, USA modified from Ellis et al. (2015). Ignimbrites indicated in gray.

861 Figure 2: (A) Illustrative section of fracture patterns with field observations and
862 corresponding sampling sites. Field photos of Whakamaru welded ignimbrite at Maraetai
863 Dam illustrating (B) horizontal fracturing at sampling site 16MD-4 and (C) vertical fracturing
864 at sampling site 16MD-8 (examples of fracture patterns highlighted by white arrows).

865 Figure 3: AMORPH calibration curve for crystallinity measurements. Actual crystallinity (y-
866 axis) from weighed components of amorphous glass and mineral powders. Error bars on data
867 points represent one standard deviation of repeated cycles of AMORPH pattern
868 deconvolution and resultant crystallinity determination (Rowe and Brewer 2018). The third-
869 order polynomial best fit line accounts for peak overlap at high crystallinity and increased
870 difficulty distinguishing signal from noise at low crystallinity.

871 Figure 4: Low and high magnification SEM BSE images of Whakamaru groundmass textures
872 from samples 16MD-12 (55 m; A-B), 16MD-9 (49 m; C-D), 16MD-5 (20 m; E-F), and
873 16MD-2 (5 m; G-H). White arrows in (B) and (H) denote vapor-phase crystallization within
874 void spaces, while arrows in (F) denote examples of devitrification.

875 Figure 5: Low and high magnification SEM BSE images of Bishop section G groundmass
876 textures from samples BR083 (86 m; A-B), BR086 (76 m; C-D), and BR089 (56 m; E-F).
877 Arrows in (A) denote vapor-phase crystallization along pumice clast margins, while (D)

878 exemplifies devitrification. White arrows in (E) point out examples of "silica streamers" as
879 discussed in the text.

880 Figure 6: BSE images through the Grey's Landing section demonstrating the coarsening of
881 texture towards the interior of the flow. Images were collected at 4 m (A), 8 m (B), 16 m (C),
882 24 m (D), 36 m (E), and 48 m (F). Relatively coarse alkali feldspar and silica phases are
883 annotated in (D) while alignment (foliation) of oxide phases is annotated in (F). The scale bar
884 in all images is 10 μm.

885 Figure 7: (A) Enlargement of key peaks associated with tridymite from X-ray diffraction
886 patterns for Whakamaru samples (20-22.5° 2Θ) illustrating changing peak heights of
887 tridymite and cristobalite diffraction peaks as proportions change. (B) Rietveld refinement
888 results for silica polymorphs cristobalite and tridymite demonstrating the decrease in
889 cristobalite with increasing tridymite in 1:1 proportions for all three tridymite-bearing
890 sections.

891 Figure 8: Representative X-ray diffraction patterns from (A) the Whakamaru ignimbrite and
892 (B-D) Bishop sections G, H, and B. Diffraction patterns in red are from the contact between
893 major flow packages, or in the case of the Whakamaru ignimbrite, horizontal fracturing.
894 Diffraction patterns in black are stratigraphically below flow package contacts, and in grey
895 are above the contacts. Diffraction patterns are arbitrarily offset for viewing but have the
896 same scale. Dashed lines indicate the key tridymite diffraction peak used to identification at
897 20.6° 2Θ. Dotted lines in (A) and (D) refer to cristobalite 100% intensity (100%I) and 14%
898 intensity (14%I) peaks at 21.947° and 36.056° 2Θ, respectively.

899 Figure 9: Density, groundmass crystallinity (C_{gm}), and relative proportions of tridymite and
900 cristobalite (T/C) with stratigraphic height for the Bishop Tuff section G (A-C), and
901 Whakamaru ignimbrite (D-F). Only groundmass crystallinity and T/C are presented for the

902 Grey's Landing ignimbrite (G-H) as corresponding density measurements are not available.
903 Tridymite zones are indicated in blue. Red stars indicate samples with corresponding BSE
904 images in Figs. 7-9. Long-dashed lines in A-C and D-F represent inferred lithologic contacts,
905 while the short-dashed line (D-F) represents the region of horizontal fracturing (see text for
906 more details). Ignimbrite emplacement units defined in Wilson and Hildreth (2003) and
907 Martin (1965) and summarized in supplemental figure 1. Density measurements from Bishop
908 section G from Wilson and Hildreth (2003).

909 Figure 10: Corresponding density and groundmass crystallinity (C_{gm}) measurements versus
910 stratigraphic height for the Bishop sections H (A-B), and B (C-D). Long-dashed lines
911 represent inferred lithologic contacts with ignimbrite and fall deposit nomenclature from
912 Wilson and Hildreth (2003) and summarized in supplemental figure 1. Density measurements
913 for Bishop sections from Wilson and Hildreth (2003).

914 Figure 11: Illustrative stratigraphic models of the Grey's Landing (A), Whakamaru (B), and
915 Bishop (C) ignimbrites, with major deformation or structural features indicated with
916 corresponding zones of tridymite crystallisation (blue). The Grey's Landing ignimbrite
917 schematic column is modified from Andrews and Branney (2011), while the Whakamaru
918 column is modified from Martin (1965) and Brown et al. (1998). The dashed line in (B)
919 represents the break in stratigraphy between before the upper Whakamaru flow package.
920 Estimated magmatic temperatures from Fe-Ti oxides (see text for details and references).

921

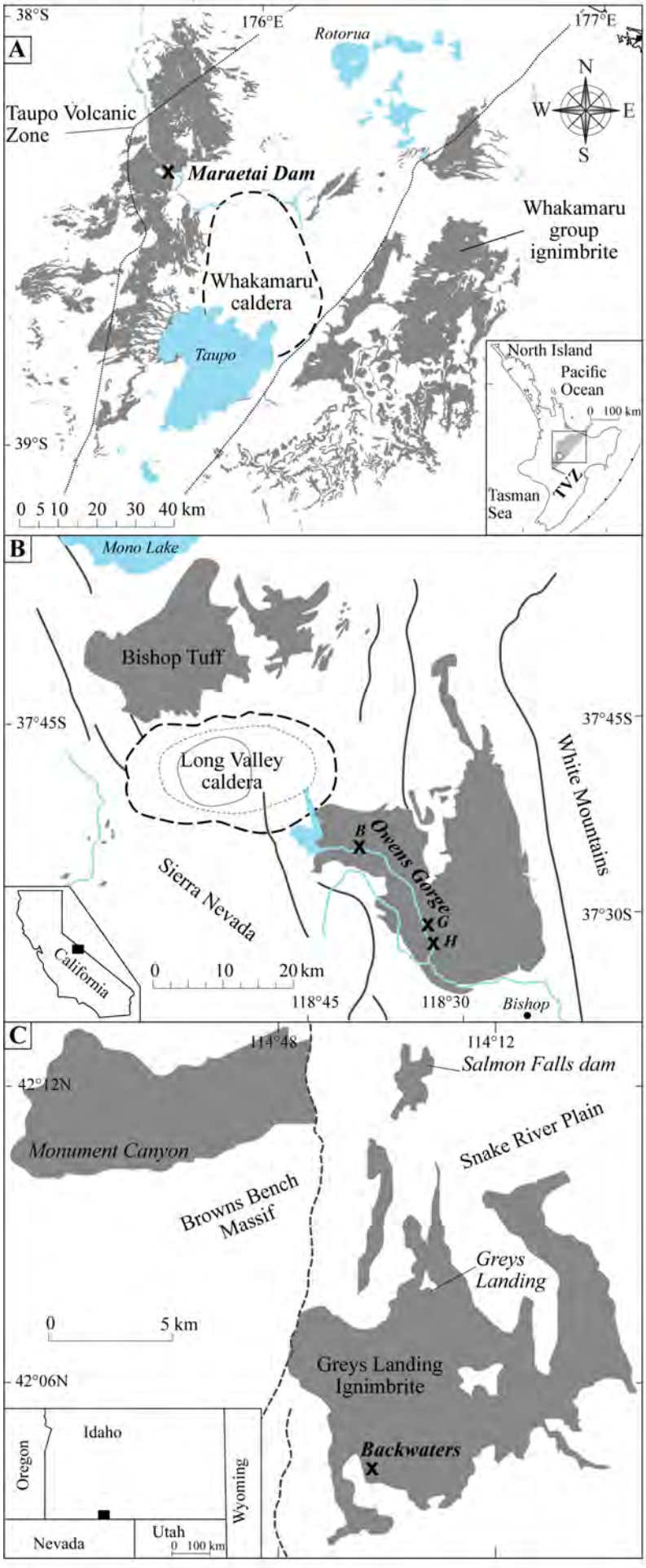
A
38°S
176°E
177°E
Rotorua
Taupo Volcanic Zone
Maraetai Dam
Whakamaru caldera
Whakamaru group ignimbrite
Taupo
39°S
0 5 10 20 30 40 km
N
W
E
S
North Island
Pacific Ocean
0 100 km
TVZ
Tasman Sea
B
Mono Lake
Bishop Tuff
37°45S
Long Valley caldera
Owens Gorge
B
G
H
Sierra Nevada
White Mountains
37°30S
California
0 10 20 km
118°45
118°30
Bishop
C
114°48
114°12
Salmon Falls dam
42°12N
Monument Canyon
Snake River Plain
Browns Bench Massif
Greys Landing
0 5 km
42°06N
Greys Landing Ignimbrite
Backwaters
Idaho
Oregon
Wyoming
Nevada
Utah
0 100 km

Figure 1

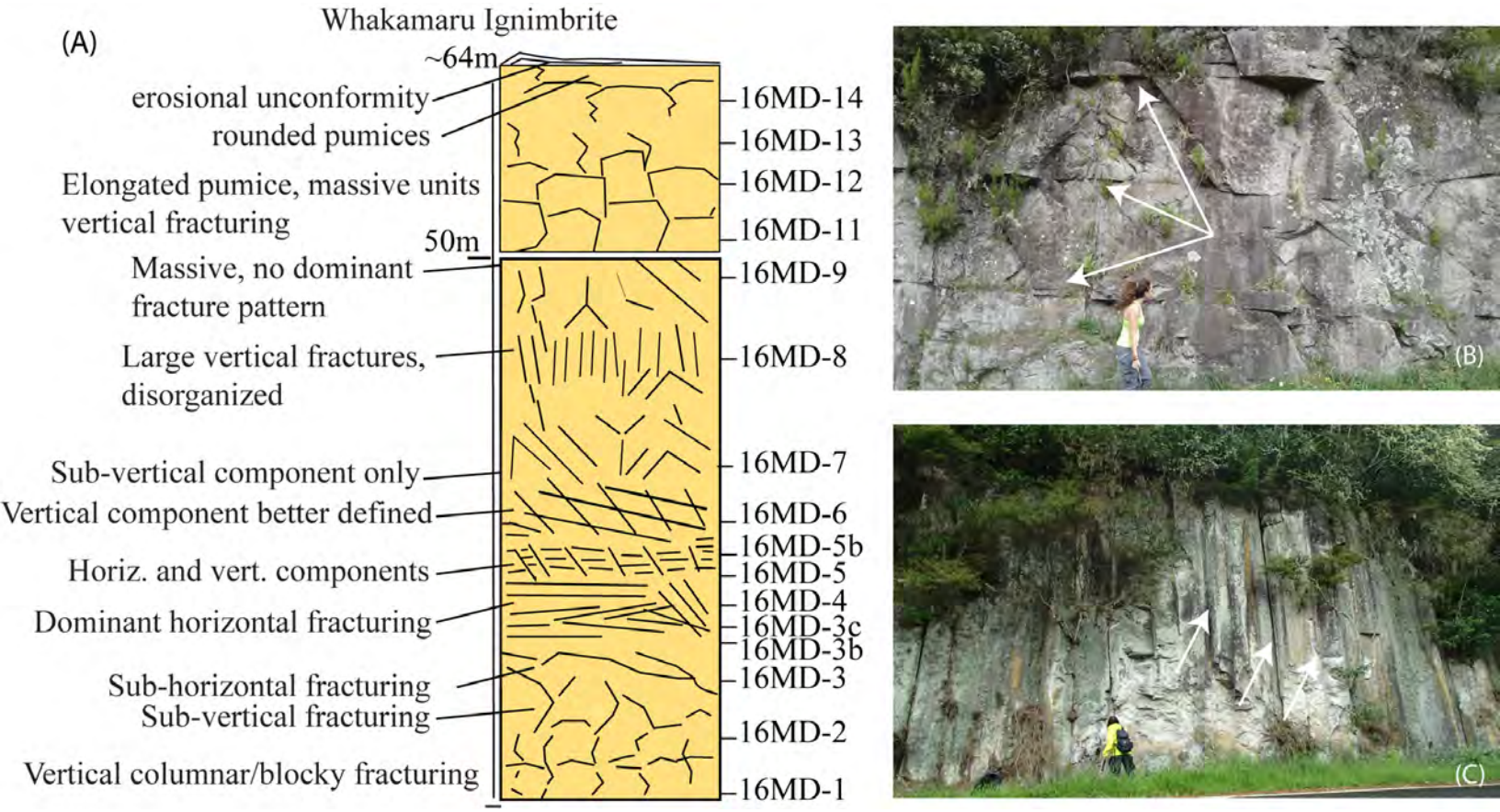
(A)
Whakamaru Ignimbrite
~64m
erosional unconformity
rounded pumices
Elongated pumice, massive units
vertical fracturing
50m
Massive, no dominant
fracture pattern
Large vertical fractures,
disorganized
Sub-vertical component only
Vertical component better defined
Horiz. and vert. components
Dominant horizontal fracturing
Sub-horizontal fracturing
Sub-vertical fracturing
Vertical columnar/blocky fracturing
16MD-14
16MD-13
16MD-12
16MD-11
16MD-9
16MD-8
16MD-7
16MD-6
16MD-5b
16MD-5
16MD-4
16MD-3c
16MD-3b
16MD-3
16MD-2
16MD-1
(B)
(C)

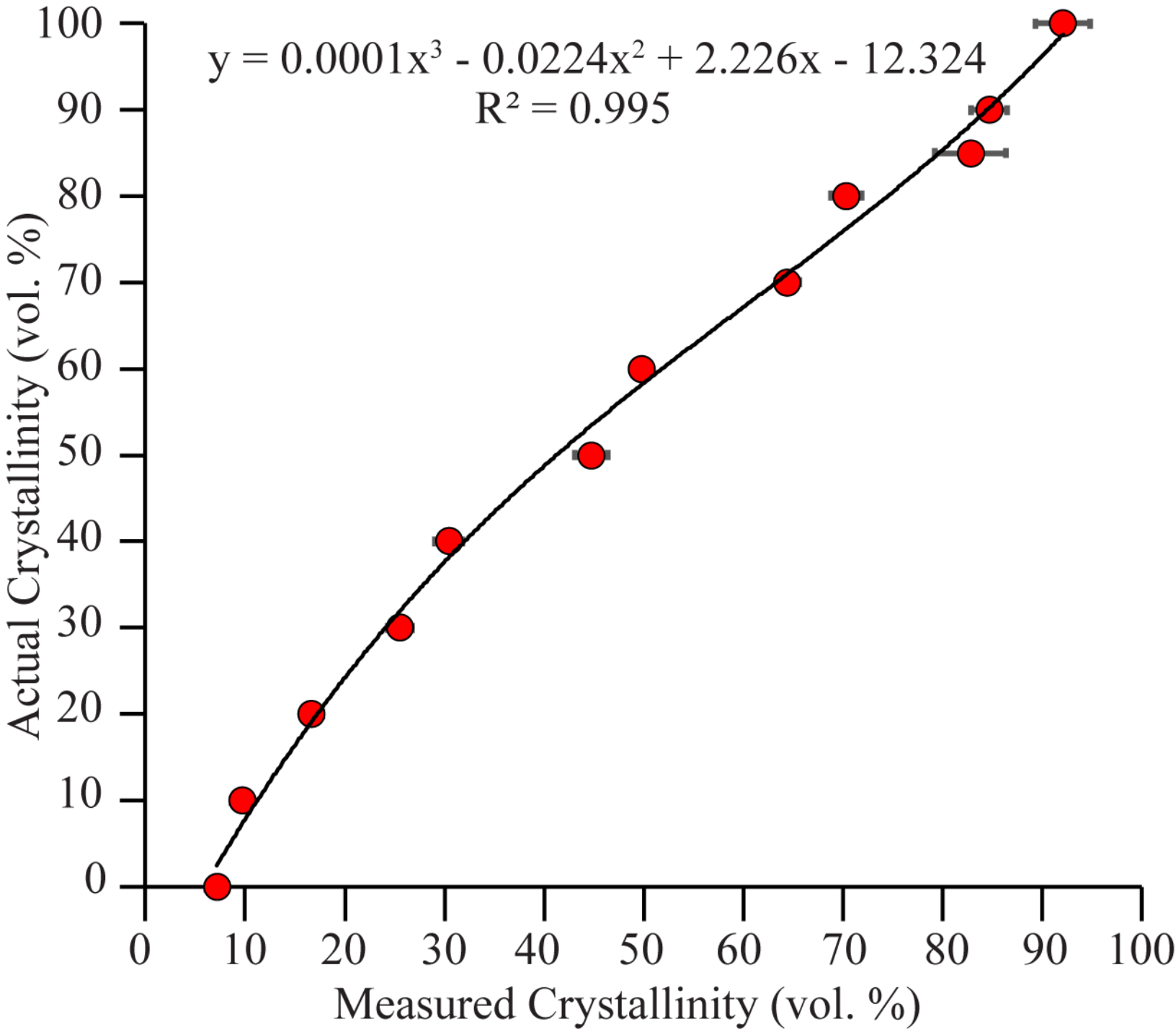
y = 0.0001x³ - 0.0224x² + 2.226x - 12.324
R² = 0.995
Actual Crystallinity (vol. %)
Measured Crystallinity (vol. %)
0
10
20
30
40
50
60
70
80
90
100

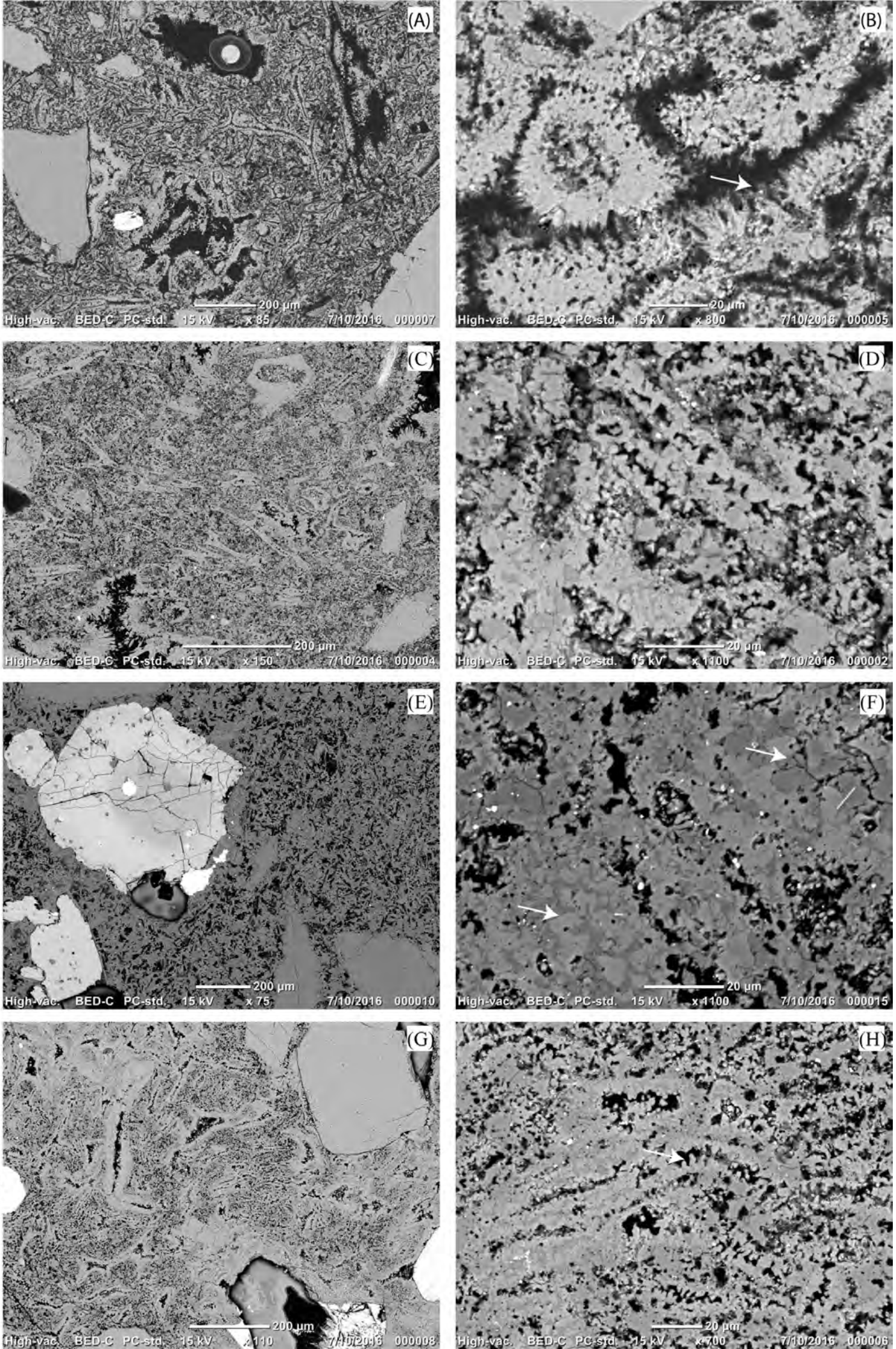
16MD-12
16MD-9
16MD-5
16MD-2
(A)
200 µm
High-vac. BED-C PC-std. 15 kV x 85 7/10/2016 000007
(B)
20 µm
High-vac. BED-C PC-std. 15 kV x 800 7/10/2016 000005
(C)
200 µm
High-vac. BED-C PC-std. 15 kV x 150 7/10/2016 000004
(D)
20 µm
High-vac. BED-C PC-std. 15 kV x 1100 7/10/2016 000002
(E)
200 µm
High-vac. BED-C PC-std. 15 kV x 75 7/10/2016 000010
(F)
20 µm
High-vac. BED-C PC-std. 15 kV x 1100 7/10/2016 000015
(G)
200 µm
High-vac. BED-C PC-std. 15 kV x 110 7/10/2016 000008
(H)
20 µm
High-vac. BED-C PC-std. 15 kV x 700 7/10/2016 000006

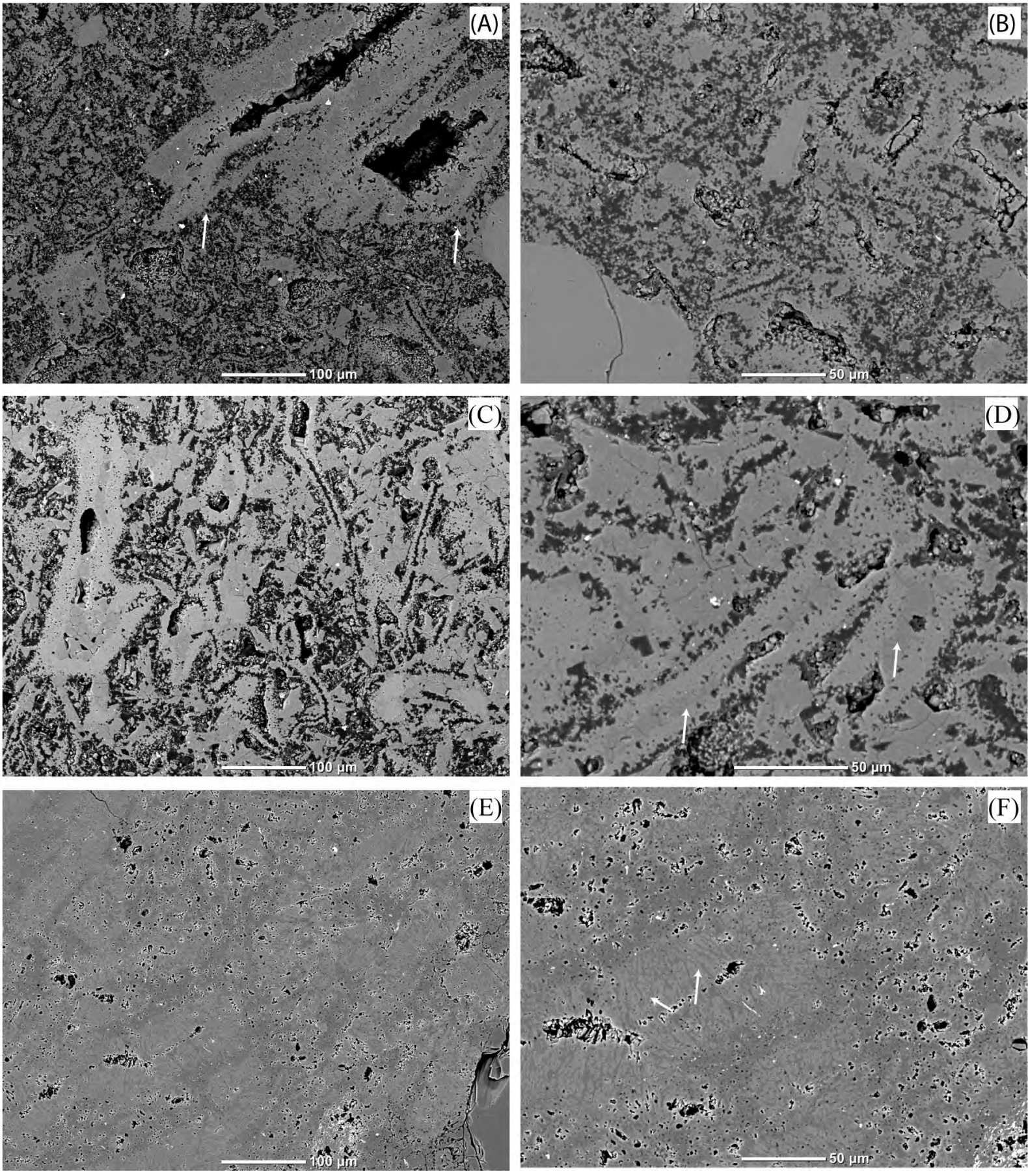
BR083
BR086
BR089
(A)
100 µm
(B)
50 µm
(C)
100 µm
(D)
50 µm
(E)
100 µm
(F)
50 µm

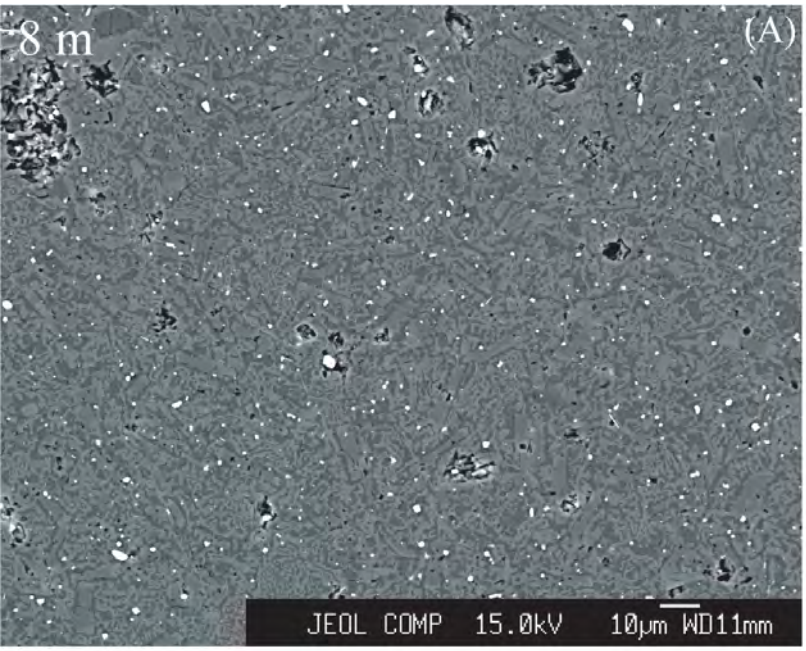
8 m
(A)
JEOL COMP 15.0kV 10μm WD11mm

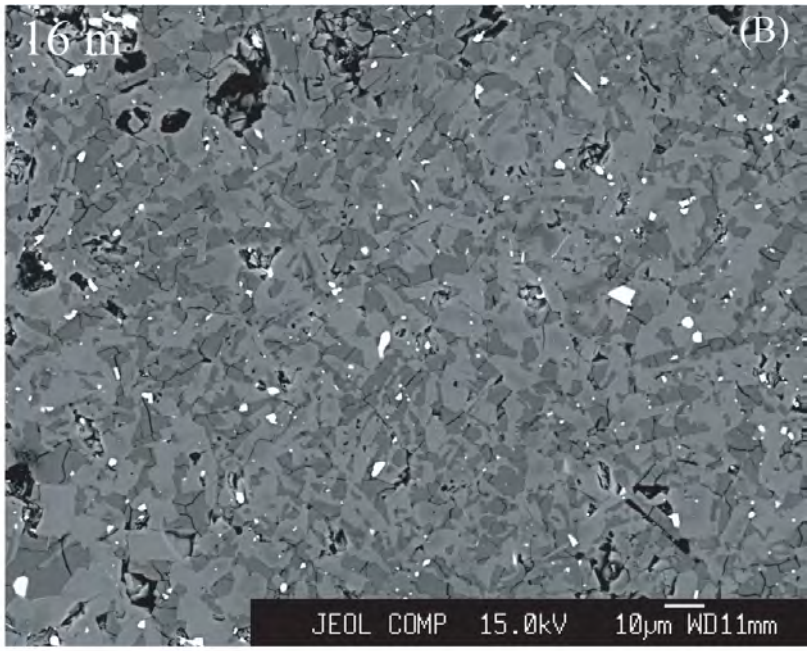
16 m
(B)
JEOL COMP 15.0kV 10μm WD11mm

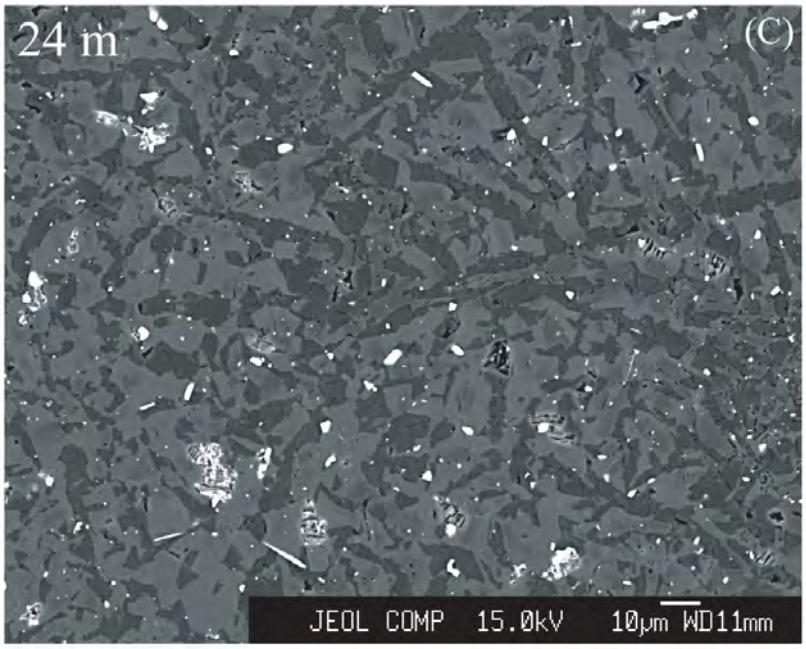
24 m
(C)
JEOL COMP 15.0kV 10μm WD11mm

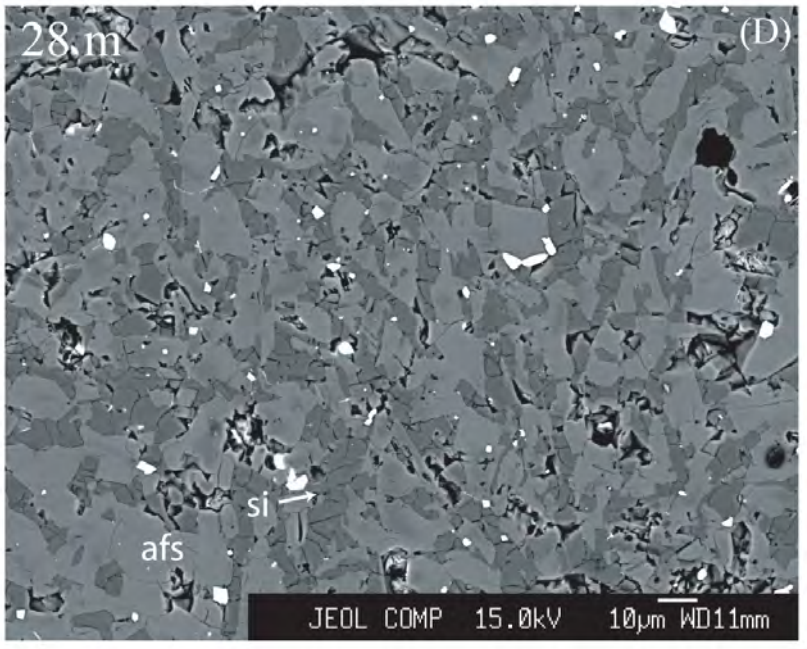
28 m
(D)
si
afs
JEOL COMP 15.0kV 10μm WD11mm

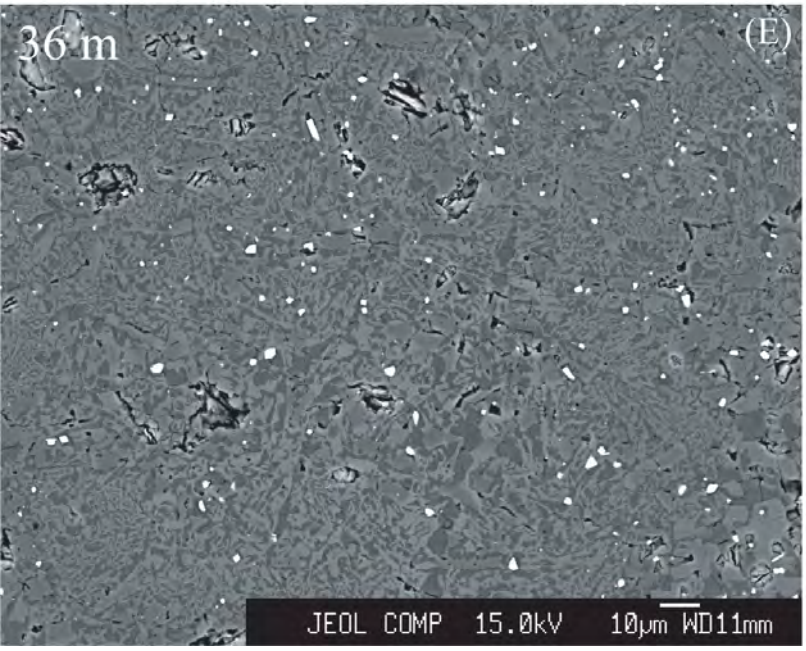
36 m
(E)
JEOL COMP 15.0kV 10μm WD11mm

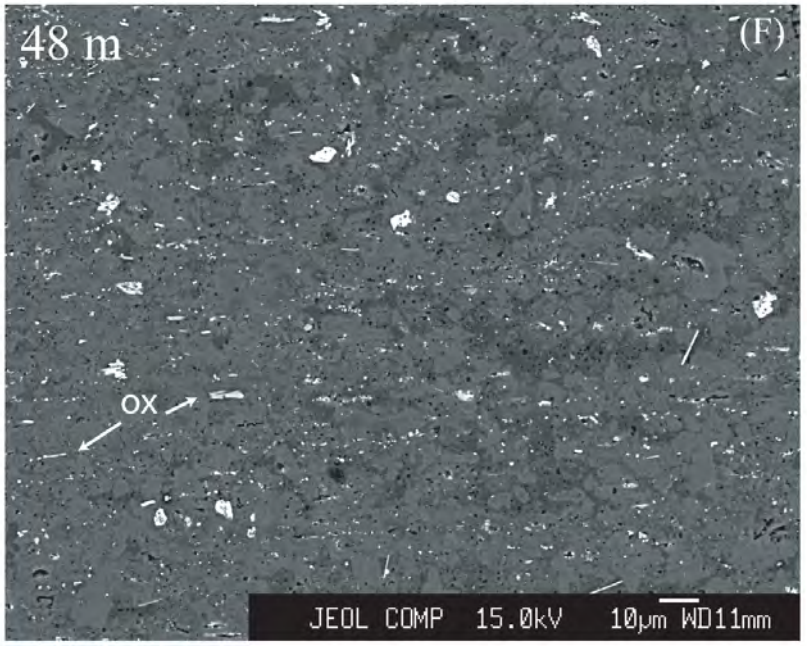
48 m
(F)
ox
JEOL COMP 15.0kV 10μm WD11mm

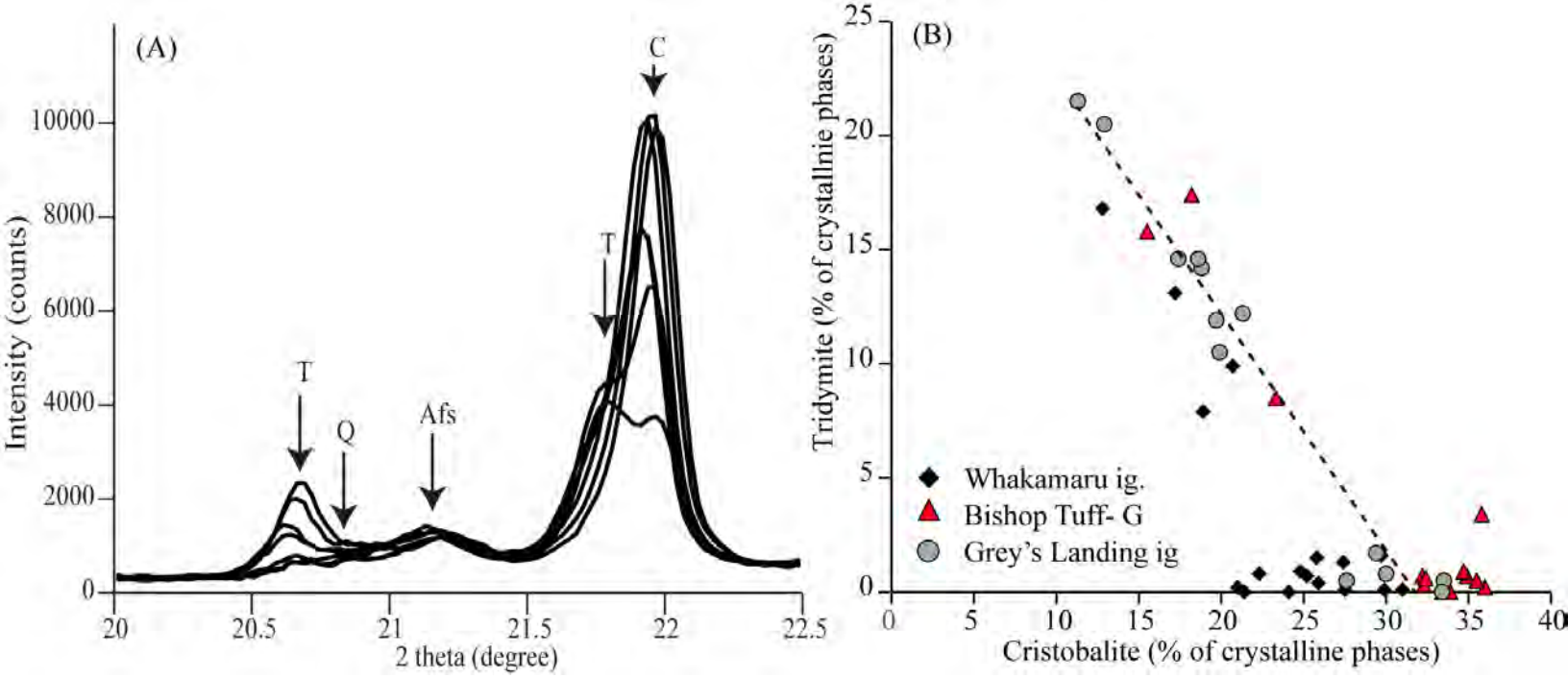
(A)
C
T
T
Q
Afs
Intensity (counts)
10000
8000
6000
4000
2000
0
20
20.5
21
21.5
22
22.5
2 theta (degree)
(B)
Tridymite (% of crystallnie phases)
25
20
15
10
5
0
0
5
10
15
20
25
30
35
40
Cristobalite (% of crystalline phases)
Whakamaru ig.
Bishop Tuff- G
Grey's Landing ig

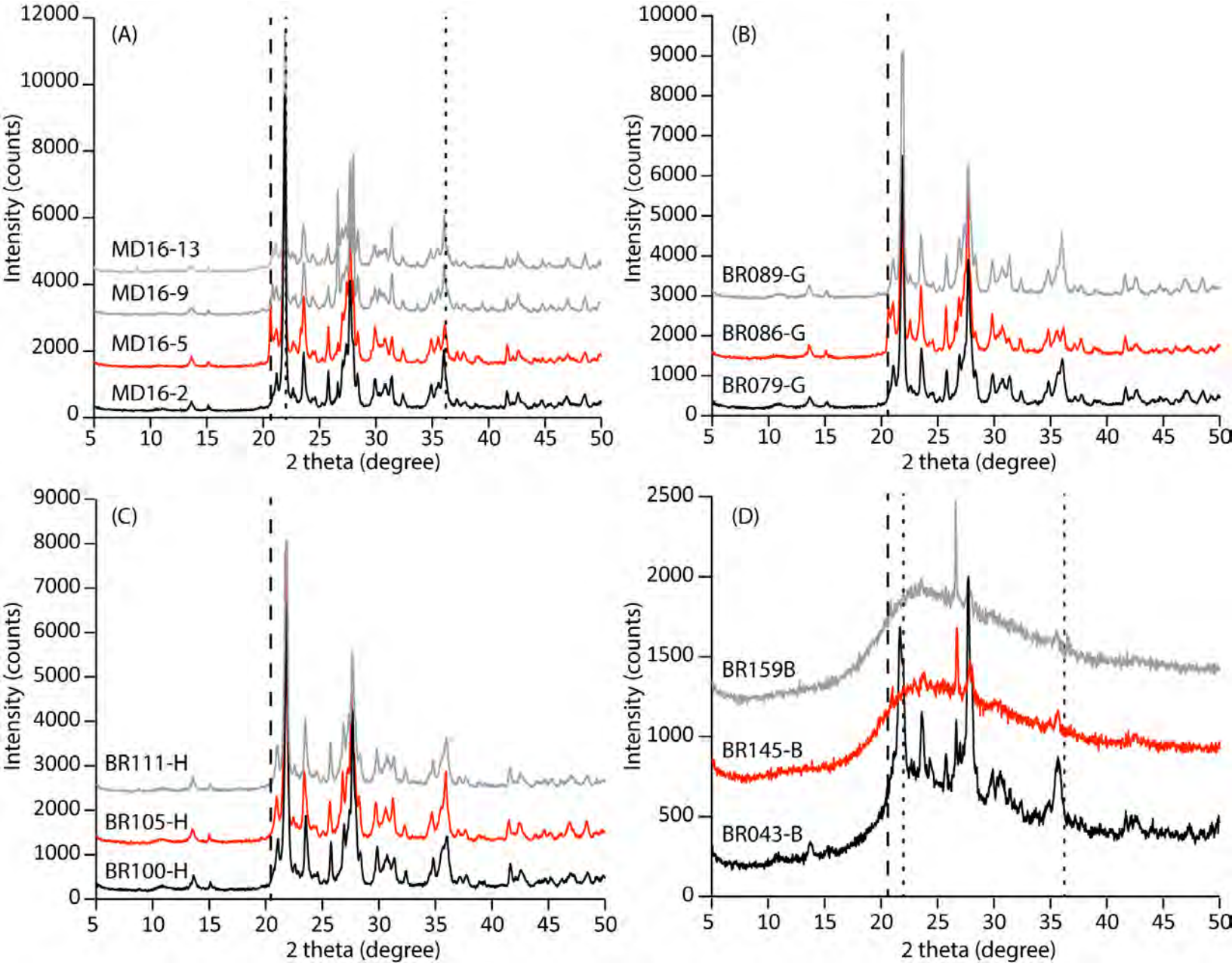
(A)
MD16-13
MD16-9
MD16-5
MD16-2
Intensity (counts)
2 theta (degree)
(B)
BR089-G
BR086-G
BR079-G
Intensity (counts)
2 theta (degree)
(C)
BR111-H
BR105-H
BR100-H
Intensity (counts)
2 theta (degree)
(D)
BR159B
BR145-B
BR043-B
Intensity (counts)
2 theta (degree)

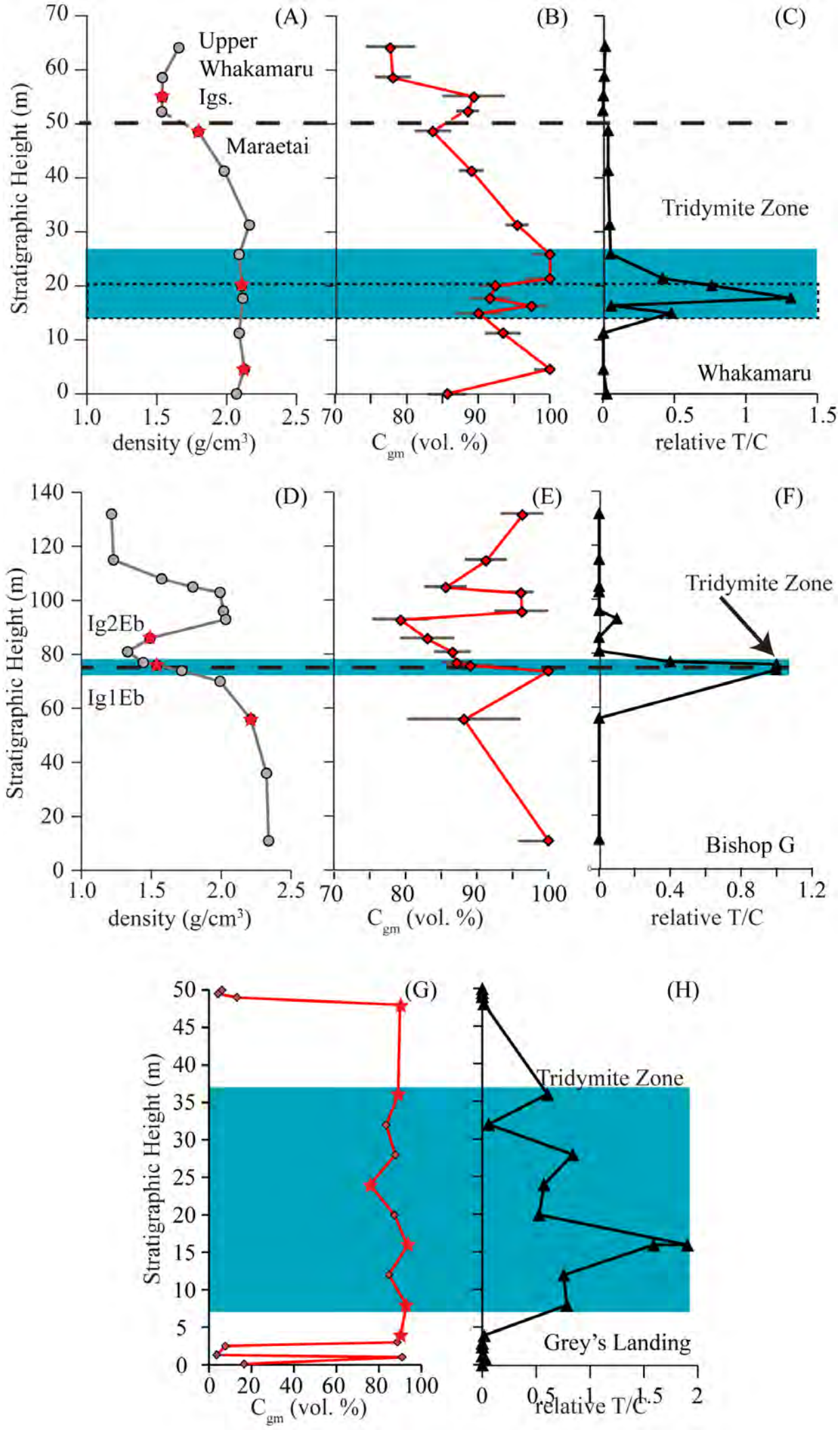
(A)
(B)
(C)
Upper
Whakamaru
Igs.
Maraetai
Tridymite Zone
Whakamaru
Stratigraphic Height (m)
density (g/cm³)
C_gm (vol. %)
relative T/C
(D)
(E)
(F)
Ig2Eb
Ig1Eb
Tridymite Zone
Bishop G
(G)
(H)
Tridymite Zone
Grey's Landing

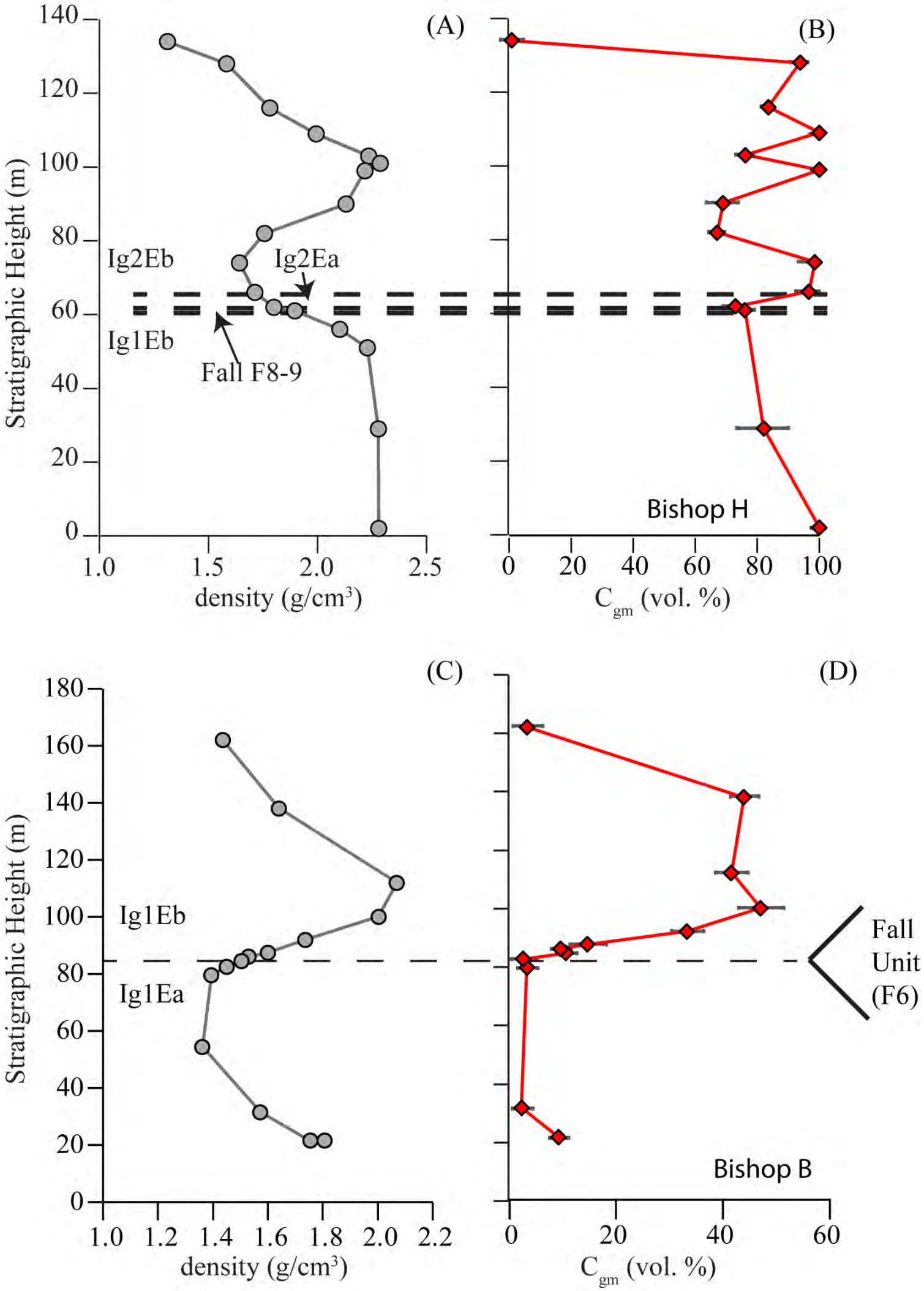
(A)
(B)
(C)
(D)
Stratigraphic Height (m)
Ig2Eb
Ig2Ea
Ig1Eb
Fall F8-9
Bishop H
density (g/cm³)
C_gm (vol. %)
Ig1Eb
Ig1Ea
Fall
Unit
(F6)
Bishop B
density (g/cm³)
C_gm (vol. %)

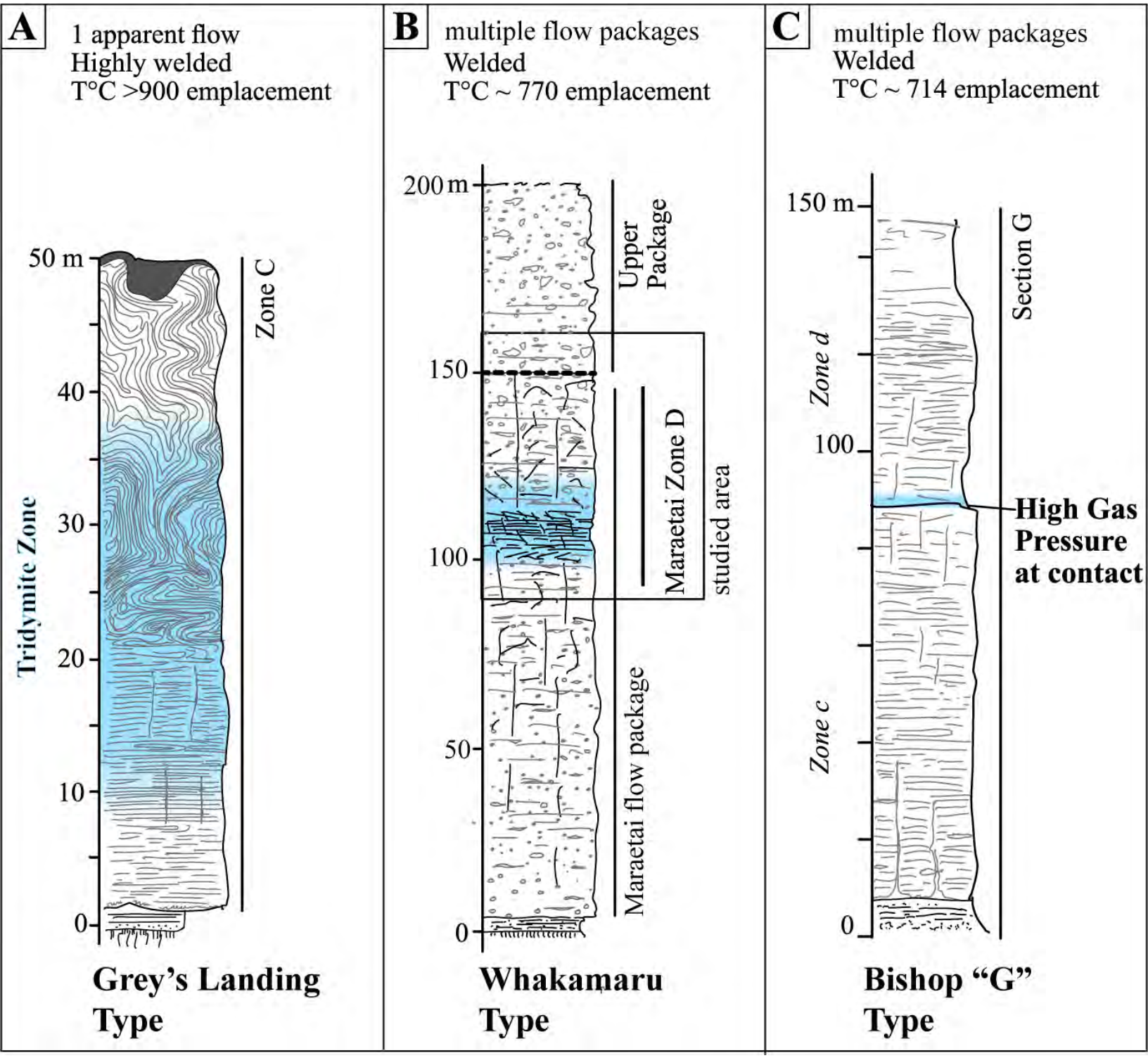
A
1 apparent flow
Highly welded
T°C >900 emplacement
50 m
40
30
20
10
0
Tridymite Zone
Zone C
Grey's Landing Type
B
multiple flow packages
Welded
T°C ~ 770 emplacement
200 m
150
100
50
0
Upper Package
Maraetai Zone D
studied area
Maraetai flow package
Whakamaru Type
C
multiple flow packages
Welded
T°C ~ 714 emplacement
150 m
100
0
Zone d
Zone c
Section G
High Gas Pressure at contact
Bishop "G" Type

Table 1: Summary of density and XRD results for the Whakamaru ignimbrite, Bishop Tuff section (G), and Grey's La

	strat. m	density g/cm^3	C_{gm}	C_{gm} SD	Crs %	Trd %	T/C	
Whakamaru ignimbrite								
16MD-14	64	1.66	0.78	0.03	21.1	0.3	0.0	
16MD-13	59	1.54	0.78	0.02	17.1	0.2	0.0	
16MD-12	55	1.54	0.89	0.04	24.4	0.1	0.0	
16MD-11	52	1.53	0.89	0.01	18.8	0.0	0.0	
16MD-10		1.33	1	0.02	23.8	0.0	0.0	
16MD-9	49	1.80	0.84	0.02	21.1	0.8	0.0	
16MD-8	41	1.98	0.89	0.02	19.7	0.7	0.0	
16MD-7	31	2.16	0.95	0.01	25.2	1.2	0.0	
16MD-6	26	2.09	1	0.02	29.0	1.6	0.1	
16MD 5b	21	--	1	0.03	17.9	7.5	0.4	
16MD-5	20	2.11	0.92	0.02	15.5	11.8	0.8	
16MD-4	18	2.12	0.92	0.03	11.5	15.1	1.3	
16MD 3c	16	--	0.97	0.02	24.0	1.4	0.1	
16MD 3b	15	--	0.90	0.03	18.4	8.8	0.5	
16MD-3	11	2.09	0.93	0.02	27.2	0.1	0.0	
16MD-2	5	2.13	1	0.02	29.4	0.1	0.0	
16MD-1	0	2.07	0.86	0.03	21.8	0.6	0.0	
Bishop Tuff Section G[1]								
BR076 G	132	1.22	0.96	0.03	32.2	0.6	0.0	
BR077 G	115	1.23	0.91	0.03	28.9	0.3	0.0	
BR079 G	105	1.80	0.86	0.03	31.1	0.2	0.0	
BR080 G	103	1.99	0.96	0.02	32.0	0.8	0.0	
BR081 G	96	2.02	0.96	0.04	32.8	0.5	0.0	
BR082 G	93	2.03	0.79	0.04	29.5	2.8	0.1	
BR083 G	86	1.49	0.83	0.04	27.3	0.6	0.0	
BR084 G	81	1.33	0.87	0.02	28.2	0.5	0.0	
BR085 G	77	1.44	0.87	0.02	20.3	7.4	0.4	
BR086 G	76	1.54	0.89	0.03	16.1	15.4	1.0	
BR087 G	74	1.72	1	0.03	15.3	15.6	1.0	
BR089 G	56	2.21	0.88	0.08	29.4	0.0	0.0	
BR091G	11	2.34	1	0.04	32.2	0.0	0.0	
Grey's Landing Ignimbrite[2]								
11-031	50		0.06	--	--	--		
11-032	49.5		0.04	--	--	--		
11-033	49		0.13	--	--	--		
11-034	48		0.90		30.1	0.4	0.0	
11-051	36		0.89		17.5	10.6	0.6	
11-050	32		0.83		24.5	1.4	0.1	
11-049	28		0.88		15.3	12.8	0.8	
11-048	24		0.76		16.2	9.3	0.6	
11-047	20		0.87		17.4	9.2	0.5	
11-046	16		0.93		10.5	20.1	1.9	

11-046ii	16	0.94		12.1	19.2	1.6
11-045	12	0.85		15.9	12.0	0.8
11-044	8	0.93		17.3	13.6	0.8
11-041	4	0.90		24.9	0.5	0.0
11-040	3	0.89		29.6	0.0	0.0
11-039	2.5	0.08	--	--	--	
11-038	1.3	0.04	--	--	--	
11-037	1	0.91		27.3	0.7	0.0
11-036	0.1	0.16	--	--	--	

Note: C_{gm} (groudmass crystallinity) and C_{gm} standard deviation (SD) in volume fractions. Cristobalite (Crs) and tridymite (Trd) proportions from rietveld refinement (scaled based on calculated crystallinity). T/C is the tridymite to cristobalite ratio. [1]Density from Wilson and Hildreth (2003). [2]Crystallinity from Ellis et al (2015).

anding ignimbrite.

Table 2: Summary of density and XRD results for Bishop Tuff (B and H).

	strat. m	density[1] g/cm^3	C_{gm}	C_{gm} SD
Bishop Tuff Section H				
BR099 H	2	2.28	1	0.02
BR100 H	29	2.28	0.82	0.08
BR103 H	61	1.90	0.76	0.03
BR104 H	62	1.80	0.73	0.04
BR105 H	66	1.71	0.97	0.04
BR106 H	74	1.64	0.99	0.05
BR107 H	82	1.76	0.67	0.03
BR108 H	90	2.13	0.69	0.05
BR109 H	99	2.22	1	0.02
BR111 H	103	2.24	0.76	0.03
BR112 H	109	1.99	1	0.03
BR113 H	116	1.78	0.84	0.02
BR114 H	128	1.58	0.94	0.03
BR115 H	134	1.31	0.01	0.04
Bishop Tuff Section B				
BR144	21.5	1.806	0.09	0.02
BR149	31.5	1.57	0.02	0.02
BR145	79.5	1.39	0.03	0.02
BR146	82.5	1.45	0.03	0.02
BR147	84.5	1.50	0.11	0.02
BR040	86	1.53	0.10	0.02
BR148	87.5	1.60	0.15	0.03
BR041	92	1.74	0.33	0.03
BR042	100	2.00	0.47	0.04
BR043	112	2.07	0.42	0.03
BR044	138	1.64	0.44	0.03
BR045	162	1.44	0.03	0.03

Note: C_{gm} (groudmass crystallinity) and C_{gm} standard deviation (SD) in volume fractions. [1]Densities from Wilson and Hildreth (2003).

Table 3: XRF and LOI measurements from the Whakamaru transect at Maraetai dam.

Sample	SiO2	TiO2	Al2O3	Fe2O3	MgO	MnO	CaO	K2O
Whakamaru samples								
16MD-1	71.68	0.34	14.89	2.67	0.49	0.062	2.55	2.88
16MD-2	72.29	0.33	14.79	2.56	0.43	0.059	2.43	2.93
16MD-3	72.89	0.32	14.68	2.53	0.44	0.058	2.32	3.01
16MD-4	72.63	0.32	14.44	2.53	0.45	0.055	2.30	3.03
16MD-5	72.06	0.33	14.76	2.55	0.45	0.054	2.40	2.99
16MD-6	72.48	0.35	15.16	2.68	0.43	0.057	2.02	3.22
16MD-7	72.78	0.32	14.53	2.45	0.45	0.053	2.36	3.02
16MD-8	72.48	0.33	14.78	2.61	0.46	0.066	2.48	2.80
16MD-9	72.89	0.30	14.90	2.47	0.31	0.065	2.05	3.15
16MD-11	72.35	0.32	14.66	2.59	0.38	0.063	2.31	3.02
16MD-12	72.55	0.32	14.61	2.57	0.51	0.064	2.26	3.46
16MD-13	73.28	0.31	14.95	2.51	0.37	0.064	2.11	3.17
16MD-14	72.94	0.33	15.15	2.63	0.42	0.065	2.14	3.15
standards								
OU-1	58.21	0.427	14.99	8.83	4.554	0.123	6.4	0.21
SY-2	59.81	0.13	11.97	6.18	2.558	0.303	7.9	4.46
SY-2	59.67	0.132	11.9	6.19	2.567	0.304	7.89	4.44

Na2O	P2O5	LOI	Total
4.18	0.072	0.89	99.80
4.14	0.063	0.67	100.03
4.09	0.062	0.75	100.40
4.10	0.065	0.69	99.92
4.16	0.061	0.45	99.81
3.76	0.024	2.16	100.18
4.16	0.063	0.64	100.19
4.06	0.064	0.95	100.13
3.70	0.032	1.67	99.86
4.37	0.059	1.47	100.11
4.80	0.062	3.39	101.21
3.76	0.024	2.11	100.54
3.70	0.053	2.35	100.58
2.43	0.044	3.28	99.56
4.22	0.43	1.054	99.35
4.23	0.429	1.054	99.13